J. Fluid Mech. (2004), *vol.* 507, *pp.* 213–253.
DOI: 10.1017/S0022112004008286 Printed in the United Kingdom

Rayleigh–Taylor turbulence: self-similar analysis and direct numerical simulations

By J. R. RISTORCELLI AND T. T. CLARK

Los Alamos National Laboratory, Los Alamos, NM 87545, USA

(Received 30 June 2003 and in revised form 18 November 2003)

Direct numerical simulations and a self-similar analysis of the single-fluid Boussinesq Rayleigh–Taylor instability and transition to turbulence are used to investigate Rayleigh–Taylor turbulence. The Schmidt, Atwood and bulk Reynolds numbers are $Sc = 1$, $A = 0.01$, $Re \leqslant 3000$. High-Reynolds-number moment self-similarity, consistent with the the energy cascade interpretation of dissipation, is used to analyse the DNS results. The mixing layer width obeys a differential equation with solution $h(t; C_o, h_0) = \frac{1}{4} C_o A g t^2 + \sqrt{A g C_o} h_0^{1/2} t + h_0$; the result for $h(t; C_o, h_0)$ is a rigorous consequence of only one ansatz, self-similarity. It indicates an intermediate time regime in which the growth is linear and the importance of a virtual origin. At long time the well-known $h \sim \frac{1}{4} C_o A g t^2$ scaling dominates. The self-similar analysis indicates that the asymptotic growth rate is not universal. The scalings of the second-order moments, their dissipations, and production–dissipation ratios, are obtained and compared to the DNS. The flow is not self-similar in a conventional sense – there is no single length scale that scales the flow. The moment similarity method produces three different scalings for the turbulence energy-containing length scale, ℓ, the Taylor microscale, λ, and the Kolmogorov dissipation scale, η. The DNS and the self-similar analysis are in accord showing $\ell \sim A g t^2$, $\lambda \sim t^{1/2}$ and $\eta \sim ((A^2 g^2 / \nu^3) t)^{-1/4}$ achieving self-similar behaviour within three initial eddy turnovers of the inception of the turbulence growth phase at bulk Reynolds numbers in the range of $Re = 800$–1000 depending on initial conditions. A picture of a turbulence in which the largest scales grow, asymptotically, as t^2 and the smallest scales decrease as $t^{-1/4}$, emerges. As a consequence the bandwidth of the turbulence spectrum grows as $t^{9/4}$ and is consistent with the $R_t^{3/4}$ Kolmogorov scaling law of fully developed stationary turbulent flows. While not all moments are consistent, especially the dissipations and higher-order moments in the edge regions, with the self-similar results it appears possible to conclude that: (i) the turbulence length scales evolve as a power of $h(t; C_o, h_0)$; (ii) α, as demonstrated mathematically for self-similar Rayleigh–Taylor turbulence and numerically by the DNS, is not a universal constant; (iii) there is statistically significant correlation between decreasing α and lower low-wavenumber loading of the initial spectrum.

1. Introduction

The instability and transition to turbulence of an incompressible miscible fluid subject to an acceleration in a direction opposite to its density gradient is studied. The Rayleigh–Taylor instability, Sharp (1984), occurs in a wide range of engineering flows accelerating systems with heat transfer laser fusion targets, such as ocean flows and the unstable atmospheric boundary layer. Models used to understand this flow

are typically theoretical models based on physical insight (Sharp 1984), variants of the socalled k–ε turbulence models (Gauthier & Bonnet 1990; Youngs 1984, 1989, 1994), and more recently direct numerical simulation (Linden, Redondo & Youngs 1994; Dalziel, Linden & Youngs 1999; Cook & Dimotakis 2001; Young *et al.* 2001). Good historical summaries of Rayleigh–Taylor simulations are given in recent articles by Dalziel *et al.* (1999) and Young *et al.* (2001).

The focus of this article is a detailed investigation of the Rayleigh–Taylor turbulence itself and not the more usual metrics (though they are also treated) such as the mean concentration, α, the mixing layer growth rate and the molecular mixing parameter. To this end the second-order moments and diverse turbulence length scales discussed in introductory texts on turbulence, such as Tennekes & Lumley (1972), Pope (2000), are studied. Such a study is, of course, stimulated by the fact that Rayleigh–Taylor turbulence does not fall into the homogeneous, quasi-equilibrium, quasi-isotropic, shear-driven category of turbulent flows about which much (at least phenomenologically) is known. One has here an inhomogeneous, anisotropic, non-stationary turbulence driven by an active scalar in which the major production mechanism is the mean concentration gradient. It is therefore essential to understand the phenomenological differences and similarities between Rayleigh–Taylor turbulence and the more conventional stationary 'Kolmogorovian' form of turbulence, see Tennekes & Lumley (1972), Pope (2000). It seems that a basic study of Rayleigh–Taylor turbulence flow physics is necessary. To this end the second-moment equations (Tennekes & Lumley 1972), are used to suggest the quantities most relevant to describing the physics of the Rayleigh–Taylor transition and turbulence. The second-moment equations, a direct consequence of Navier–Stokes, are an exact albeit unclosed set of equations describing the laminar, transitional and turbulent states of the Rayleigh–Taylor turbulence. The second-moment equations also suggest mathematically relevant questions to submit to the direct numerical simulation from a single-point moment closures as well as a flow physics point of view.

For such a complex inhomogenous non-stationary flow a further reduction of the complexity of the system, through the application of some simplifying ansatz is useful from the viewpoint of both the turbulent flow physics as well as for turbulence modelling in moment closures and large-eddy simulation (LES). Self-similarity is sometimes used as a simplifying ansatz to understand complex turbulent flows (Tennekes & Lumley 1972; Pope 2000). Typically the first-moment equations are investigated with a gradient hypothesis for the turbulent fluxes. Such self-similar analyses of the thermal mixing layer of a passive scalar have been undertaken by Ma & Warhaft (1986); Lumley (1986) and de Bruyn Kops & Riley (2000). In these studies self-similarity of the mean scalar is seen to be possible only in the absence of molecular transport effects. Here a self-similar analysis of the *active* scalar mixing layer is undertaken. In the present configuration, the Rayleigh–Taylor mixing layer, the time derivative $\partial/\partial t$ plays the role of $U\partial/\partial x$ of the thermal mixing layer experiments. Such a flow has been addressed by Snider & Andrews (1994) for the laminar flow and transition past a splitter plate separating two fluids of different temperature.

The present investigation extends the conventional notion of self-similar analyses applied to mean equations to the second-order moment equations, thus avoiding a constant eddy diffusivity gradient transport closure in the first-moment equation. As such the invocation of diffusion as a model for turbulen transport can be avoided and a more unbiased view of Rayleigh–Taylor turbulence is possible. Furthermore, as many of the phenomenogical descriptors of turbulence and mixing occur in these equations their self-similar scalings can be used to understand the complicating issues

of the non-stationarity and inhomogeneity of Rayleigh–Taylor turbulence in the prediction of mixing.

The self-similar analysis produces ordinary differential equations for the temporal and spatial functions for the moments appearing in the second-order moment equations. One of the interesting byproducts of such an analysis, as will be seen in § 3, is a nonlinear ordinary differential equation for the planar average of the mixing layer width, $h(t; C_o, h_0)$:

$$\dot{h}^2 = Ag\, C_o\, h. \tag{1.1}$$

The equation is a rigorous consequence of Navier–Stokes formulation with only the one ansatz of self-similarity. As an exact mathematical result it validates the structure of more heuristically derived equations (Sharp 1984; Cook & Dimotakis 2001), using phenomenological buoyancy–drag type models. One of the important questions in Rayleigh–Taylor turbulence is the dependence on the initial conditions of the turbulent phase of the growth. A recent summary of this topic can be found in Young *et al.* (2001). Additional more specialized discussions can be found in Dalziel *et al.* (1999) or Cook & Dimotakis (2001). The self-similar analysis presented highlights the fact that even in the most ideal of circumstances (self-similarity) the asymptotic growth rate is a function of the solution of the spatial profiles of an unclosed set of moment equations. Solutions to the above mixing layer width equation and connections between α and C_o and the initial conditions dependence of the asympotic growth rate are discussed in § 3. Cook & Dimotakis (2001) have in addition pointed out that the mixing is more sensitive to initial conditions than the mixing layer width.

As has been mentioned the anisotropy, inhomogeneity, non-stationarity and buoyancy of Rayleigh–Taylor turbulence distinguish it in non-trivial ways from the turbulence ideal of Kolmogorov that finds application to stationary high-Reynolds-number shear-driven flows. The hallmark of this latter category of flows is their stationarity and the constancy of the net spectral flux through the inertial range to smaller scales. It is for this reason that LES has been nominally successful in capturing such flows in simple situations away from boundaries: if the large-scale end of the cascade is captured, the proverbial rate limiting step, then the smallest scales dissipating the energy need not be computed. Rayleigh–Taylor (RT) turbulence, due to its non-stationarity and cascade to larger scales, is expected to be different. To this end we present archival data that may be useful in assessing coarse-grained numerical procedures. Those data, typically lower-order moments, that coarse-grained simulations are expected to compute are highlighted in § 7.

The word 'turbulence' has been used: it is probably more precise to use the word 'stochastic' implying, in either case, a spectrum of fluctuations interacting nonlinearly through the fluctuating strain field. In such a flow the spatial and temporal two-point correlations decay and have bounded integrals. The word turbulence is colloquially used for spectra that are broadbanded and featureless and associated with high Reynolds number. In these simulations the outer-scale Reynolds number is low, $0 < Re < 3000$. In either case we shall use the word turbulence.

A brief outline of the paper is now given. First, in § 2, the governing instantaneous and moment equations are given. In § 3 the moment self-similarity analysis is undertaken and issues already highlighted are amplified. In § 4 the turbulence phenomenology suggested by the self-similar analysis is discussed using standard turbulence diagnostics (Tennekes & Lumley 1972; Pope 2000). The numerical method and initial conditions are given in the Appendix. Sections 5 and 6 present the results and comparisons to the self-similar results. Section 7 summarizes our results.

2. Governing equations

The initial value problem of a quiescent heavy fluid of density ρ_c overlaying a quiescent light fluid of density ρ_h is treated. This is a single-fluid problem driven by the density difference $\Delta\rho = \rho_c - \rho_h$. The buoyancy forces are treated in the Boussinesq approximation, thus $u_i{}_{,i} = 0$, and the instantaneous density is given in terms of the instantaneous scalar concentration $\rho^* = \rho_a + \frac{1}{2}\Delta\rho c^*$ where $\rho_a = \frac{1}{2}(\rho_h + \rho_c)$; thus $c^* = 2(\rho - \rho_a)/\Delta\rho$ and $-1 < c^* < 1$. A Cartesian coordinate system is used. The instantaneous governing equations, in dimensional form, are

$$\frac{\partial}{\partial t}u_i^* + u_j^* u_i^*{}_{,j} = -p^*{}_{,i} - Ag\delta_{i3}c^* + \nu u_i^*{}_{,jj}, \tag{2.1}$$

$$\frac{\partial}{\partial t}c^* + u_j^* c^*{}_{,j} = \mathscr{D}c^*{}_{,jj}, \tag{2.2}$$

where $u_i^*{}_{,jj} = \nabla^2 u_i^*$ as the commas represent differentiation. The pressure has been non-dimensionalized by ρ_a. The Atwood number is $A = (\rho_h - \rho_c)/(\rho_h + \rho_c) \ll 1$. As the problem begins in the quiescent state time, space and velocity are made non-dimensional (for the numerical problem) with scalings of the linear stability problem (Chandrasekhar 1961). The variables are made non-dimensional with the following characteristic length, time and velocity scales:

$$\ell_c = \left(\frac{\nu^2}{gA}\right)^{1/3}, \qquad t_c = \left(\frac{\nu}{g^2A^2}\right)^{1/3}, \qquad u_c = (\nu g A)^{1/3}. \tag{2.3}$$

From Chandrasekhar (1961) as quoted in Linden & Redondo (1991) the wavenumber of the most unstable mode of the linear problem (without surface tension or diffusion) is

$$\lambda_{mx} \approx 4\pi\left(\frac{\nu^2}{gA}\right)^{1/3} \Rightarrow \kappa_{mx} \approx \frac{1}{2}\left(\frac{\nu^2}{gA}\right)^{-1/3}, \qquad n_{mx} \approx \left(\frac{\pi g A}{\lambda_{mx}}\right)^{1/2} \tag{2.4}$$

using the relation $\kappa_{mx} = 2\pi/\lambda_{mx}$. With these scalings the instantaneous equations become

$$\frac{\partial}{\partial t}u_i^* + u_j^* u_i^*{}_{,j} = -p^*{}_{,i} - c^*\delta_{i3} + u_i^*{}_{,jj}, \tag{2.5}$$

$$\frac{\partial}{\partial t}c^* + u_j^* c^*{}_{,j} = \frac{\mathscr{D}}{\nu}c^*{}_{,jj}. \tag{2.6}$$

The above equation set is solved by the direct numerical simulation discussed below. The Schmidt number is $Sc = \nu/\mathscr{D}$ and $Sc = 1$ and $A = 0.01$ in all simulations.

2.1. *The moment equations*

A clear and economical characterization of the physics of the Rayleigh–Taylor flow and a useful statistical description of the numerical results can be obtained from the second-moment equations. The moment equations are derived from the governing equations, (2.5), (2.6) using the usual Reynolds decompositions of the momentum and scalar transport equations: $u_i^* = U_i + u_i$ and $c^* = C + c$ (Tennekes & Lumley 1972). Upper-case letters represent the first-order moments and lower-case the fluctuations: $\langle u_i \rangle = \langle c \rangle = 0$. The averaging procedure, indicated by the angle brackets, has a formal mathematical definition: it is the planar average $\langle \psi \rangle = (1/L^2)\int\int \psi \, \mathrm{d}x \, \mathrm{d}y$. This is different from the averaging procedure used in typical turbulence models for engineering closures and does not require stationarity. The present version of the RT problem is statistically homogeneous in the (1,2) horizontal plane and inhomogeneous

in the vertical or 3- (or z) direction. The only non-zero derivative of statistical moment is in the inhomogeneous 3- or z-direction.

There are only two non-zero first-order moments: the mean concentration C, and the mean pressure P. The first-order moment equations are

$$\langle u_3 u_3\rangle_{,3} = -P_{,3} - AgC, \qquad \frac{\partial}{\partial t}C + \langle u_3 c\rangle_{,3} = \mathscr{D}C_{,33}\,. \tag{2.7}$$

In the absence of velocity fluctuations the mean concentration balances the mean pressure and the concentration field changes by molecular diffusion only. Otherwise the balance between mean pressure and mean concentration is set by the inhomogeneity of the vertical momentum flux. The evolution of the mean concentration is determined by the scalar flux, $\langle u_3 c\rangle$. The evolution of $\langle u_3 c\rangle$ is coupled to the variances $\langle cc\rangle$ and $\langle u_3 u_3\rangle$. The second moments $\langle u_3 c\rangle, \langle cc\rangle, \langle u_3 u_3\rangle$ evolve according to

$$\frac{\partial}{\partial t}\langle u_3 c\rangle + \langle u_3 u_3 c\rangle_{,3} = -\langle u_3 u_3\rangle C_{,3} - Ag\langle cc\rangle + (\mathscr{D}+\nu)\nabla^2\langle u_3 c\rangle \\ - \langle pc\rangle_{,3} + \langle pc_{,3}\rangle - \mathscr{D}\langle u_{3,3}\, c\rangle_{,3} - \nu\langle u_3 c_{,3}\rangle_{,3} - \varepsilon_3, \tag{2.8}$$

$$\frac{\partial}{\partial t}\langle cc\rangle + \langle u_3 cc\rangle_{,3} = -2\langle u_3 c\rangle C_{,3} + \mathscr{D}\nabla^2\langle cc\rangle - 2\varepsilon_c, \tag{2.9}$$

$$\frac{\partial}{\partial t}\langle u_3 u_3\rangle + \langle u_3 u_3 u_3\rangle_{,3} = -2Ag\langle u_3 c\rangle + \nu\nabla^2\langle u_3 u_3\rangle - 2\langle u_3 p\rangle_{,3} + 2\langle p s_{33}\rangle - \varepsilon_{33}. \tag{2.10}$$

While both the diffusive transport $\mathscr{D}\nabla^2\langle cc\rangle$ and scalar dissipation ε_c reduce the scalar variance, ε_c will dominate and will be called the mixing rate. For completeness the turbulence energy equation is given:

$$\frac{\partial}{\partial t}k + \tfrac{1}{2}\langle u_3 u_j u_j\rangle_{,3} = -Ag\langle u_3 c\rangle + \nu\,\nabla^2 k - \langle p u_3\rangle_{,3} - \varepsilon. \tag{2.11}$$

The customary definitions of the dissipations have been applied:

$$\varepsilon_c = \mathscr{D}\langle c_{,j}\, c_{,j}\rangle, \qquad \varepsilon_{jj} = 2\varepsilon = \nu\langle u_{j,k}\, u_{j,k}\rangle, \tag{2.12}$$

$$\varepsilon_{ij} = 2\nu\langle u_{i,k}\, u_{j,k}\rangle, \qquad \varepsilon_i = (\nu + D)\langle c_{,j}\, u_{i,j}\rangle. \tag{2.13}$$

As the flow is not stationary and does not have a high Reynolds number the identification of the dissipation with the cascade rate is not, in principle, justified. This is especially true in the edge regions.

The second-moment equations, (2.8), (2.9), (2.10), are the equations describing the evolution of the turbulence. They describe the RT flow through all of its regimes: from its inceptional quiescent state, through the laminar state, and into the fully turbulent regime. If cubic terms are dropped the set of equations describes the moments of the linear stability problem – the stochastic nature of the flow having been introduced by the initial conditions.

3. Self-similarity analysis of the turbulence growth phase

Self-similar solutions of the form

$$F(z,t) = F_o(t) f(\eta), \qquad \eta = \frac{z}{h(t)}, \tag{3.1}$$

are assumed; $F_0(t)$ is the temporal scaling function and $f(\eta)$ is the spatial similarity function. Here $h(t)$ is the layer half-width. Any temporal function with subscript o,

e.g. F_o, associated with an even profile function, is proportional to the magnitude of the function on the $z=0$ plane. Any temporal function with subscript o, associated with an odd profile function, is determined by integrals of the profile functions. The self-similar solution forms are now applied to the first- and second-moment equations.

The mean scalar equation and its similarity groups are

$$\left[\frac{\dot{C}_o h}{C_o \dot{h}} f_C - \eta f_C'\right] + \frac{\langle u_3 c\rangle_o}{\dot{h} C_o} f_{3c}' = \frac{\mathscr{D}}{h\dot{h}} f_C''. \tag{3.2}$$

The equation is arrived at by inserting the self-similar ansatz (3.1) into the mean concentration equation, (2.7). Three different balances, leading to three different self-similar scalings, are possible for the moment equations. The turbulence growth phase is the subject of our analysis. A balance between the first two terms describes the flow in the turbulence growth phase and implies a Reynolds number high enough to neglect diffusive transport, $\mathscr{D}C_{,33}$, and similarly for transport terms involving $\mathscr{D}$ and ν in the second-moment equations. This corresponds to the notion that once the flow transitions, producing the small scales with large gradients characteristic of turbulence, molecular effects responsible for dissipation become much more important than transport by molecular effects. Transport is set by the mean gradient (which is small compared to the r.m.s. fluctuating gradients responsible for dissipation) and scales with Re^{-1}.

Following conventional self-similarity procedures one requires the coefficients of the similarity functions be constants, for example $\langle u_3 c\rangle_o / \dot{h} C_o = 1$. A solution for $h(t)$ is not specified by the first-moment equation and one requires the second-moment equations. The self-similar forms of the second-moment equations lead to a series of ordinary differential equations for the coefficient functions. Inserting the self-similar ansatz (3.1) into (2.9) the scalar variance equation and its similarity groups are written

$$\frac{\langle c\dot{c}\rangle_o h}{\langle cc\rangle_o \dot{h}} f_{cc} - \eta f_{cc}' + \frac{\langle u_3 cc\rangle_o}{\dot{h}\langle cc\rangle_o} f_{33c}' = -2\frac{\langle u_3 c\rangle_o C_o}{\dot{h}\langle cc\rangle_o} f_{3c} f_C' + \frac{\mathscr{D}}{h\dot{h}} f_{cc}'' + 2\frac{h\varepsilon_{co}}{\dot{h}\langle cc\rangle_o} f_{\varepsilon c}. \tag{3.3}$$

Combining the similarity groups from the turbulent transport term in the first-moment equation, $\langle u_3 c\rangle_o / \dot{h} C_o = 1$, and from the production term in the variance equations, $\langle u_3 c\rangle_o C_o / \dot{h}\langle cc\rangle_o = 1$, and eliminating $\langle u_3 c\rangle$ produces

$$\langle cc\rangle_o = C_o^2. \tag{3.4}$$

That $C(\pm\infty) = \pm 1$ requires $C_o = \text{const}$; thus $\langle cc\rangle_o = \text{const}$ for self-similarity. The scalar flux equation and its similarity groups are written

$$\frac{\langle u_3\dot{c}\rangle_o h}{\langle u_3 c\rangle_o \dot{h}} f_{3c}' - \eta f_{3c} + \frac{\langle u_3 u_3 c\rangle_o}{\dot{h}\langle u_3 c\rangle_o} f_{33c}' = -2\frac{\langle u_3 u_3\rangle_o C_o}{\dot{h}\langle u_3 c\rangle_o} f_{33} f_C' - Ag\frac{\langle cc\rangle_o h}{\dot{h}\langle u_3 c\rangle_o} f_{cc} + \frac{\mathscr{D}+\nu}{h\dot{h}} f_{3c}'' + \frac{h\varepsilon_{3co}}{\dot{h}\langle u_3 c\rangle_o} f_{\varepsilon 3c}. \tag{3.5}$$

The two production terms indicate $\langle u_3 u_3\rangle_o = \dot{h}\langle u_3 c\rangle_o / C_o$ and $\langle u_3 c\rangle_o = Ag\langle cc\rangle_o h/\dot{h}$.

3.1. *Ordinary differential equation for the mixing layer width*

Combining $\langle u_3 c\rangle_o = Ag\langle cc\rangle_o h/\dot{h}$, with the production group from the scalar variance equation, $\langle u_3 c\rangle_o C_o / \dot{h}\langle cc\rangle_o = 1$, produces an ordinary differential equation for the mixing layer width

$$\dot{h}^2 = Ag\, C_o h. \tag{3.6}$$

The solution is

$$h(t;, C_o, h_0) = \tfrac{1}{4}AgC_o t^2 + \sqrt{AgC_o}h_0^{1/2}t + h_0. \tag{3.7}$$

At long time the well-known empirical result, $h(t;C_o) \sim \frac{1}{4}AgC_o t^2$, emerges with $\alpha = \frac{1}{4}C_o$. The determination of C_o is discussed below. During the turbulence growth phase a linear growth regime, dependent on the initial turbulence growth phase width, h_0, is seen at short time. Departures from Agt^2 growth laws dependent on initial conditons have been noted elsewhere (Dalziel *et al.* 1999). The scaling $h = \alpha Agt^2$, appears to have first been given by Fermi (1951) for the spikes using a simple Lagrangian analysis. Youngs (1984), using physical arguments and linear stability results, has also given such a scaling. In contradistinction the result (3.7) is a rigorous mathematical consequence of the Navier–Stokes equations assuming only self-similarity for the second-order moment equations.

If one differentiates (3.7) with respect to Agt^2 one obtains an effective α:

$$\alpha_{eff} = \frac{C_o}{4}\left(1 + \sqrt{\frac{4h_0}{AgC_o t^2}}\right) \to \frac{C_o}{4}. \tag{3.8}$$

The self-similar analysis predicts an effective α that decreases with time as t^{-1}. This prediction is reminiscent of the observation of Youngs (1991) and Town & Bell (1991) that the growth rate decreases after the onset of the t^2 regime. The quantity $\frac{1}{4}C_o$ in (3.8) is identified with the traditional α, $\alpha = \frac{1}{4}C_o$, which is typically in the range $0.03 \leqslant \alpha \leqslant 0.06$ (Dimonte & Schneider 2000). The noteworthy result is that the self-similar result implies a lasting dependence on the initial conditions and not a universal asymptotic mixing layer growth rate (if the process has not reached a universal state before t_0). The quantity C_o, while in principle determinable, requires solution of spatial profiles in the unclosed set of moment equations. Consequently the asymptotic α depends on C_o which is related to various integrals of the solution. More precisely it is a functional of the solution of the self-similar moment equations; the point is moot as the equations are unclosed. Clark & Zhou (2003) show how such a relationship emerges. It is likely that C_o is very nearly the same within any one experimental situation and as such the variability of C_o is expected to be small. The reader is referred to the excellent summary regarding initial condition dependence of α in the introduction of Young *et al.* (2001).

The solution (3.7) can be written $h = h(t;h(t_0), C_o) = h(t;t_0, C_o)$ in terms of the translationally invariant group $t + t_0$. Using the non-dimensional time scale,

$$\frac{1}{t_0} = \sqrt{\frac{AgC_o}{4h_0}} \tag{3.9}$$

the solution, with $\tau = t/t_0$, becomes

$$h(t;C_o, t_0) = \frac{h_0}{t_0^2}(t + t_0)^2 = h_0(\tau + 1)^2 = \tfrac{1}{4}AgC_o t_0^2(\tau + 1)^2 \tag{3.10}$$

with a virtual origin. The point $t = t_0$ where $h = h_0$ will be called the initial condition of the turbulence growth phase or the transition condition. The time scale t_0 reflects the time scale of the fading of the portion of the mixing layer dependent on initial width; the dependence on the initial concentration field remains. The point is that a virtual origin, as is easily seen in more abstract group-theoretic methods (Clark & Zhou 2001, 2003), is an essential part of the solution. This is a well-known empirical issue in turbulence that was found to collapse the data of several apparently conflicting

experimental results on isotropic turbulence in wind tunnels (Mohamed & LaRue 1990). A solution of the form (3.10) for the mixing layer width emerges from a heuristic model for a layer growth equation reported in Cook & Dimotakis (2001) and Dimonte & Schneider (2001) as well as the group theoretic approach of Clark & Zhou (2003). Sharp (1984) gives a summary of other models for the layer.

3.2. *Temporal scalings of the moments*

The vertical momentum flux equation and its similarity groups is written

$$\frac{\langle u_3\dot{u}_3\rangle_o h}{\langle u_3u_3\rangle_o\dot{h}}f_{33}-\eta f_{33}+\frac{\langle u_3u_3u_3\rangle_o}{\dot{h}\langle u_3u_3\rangle_o}f'_{333}=-2Ag\frac{\langle u_3c\rangle_o h}{\dot{h}\langle u_3u_3\rangle_o}f_{3c}+\frac{\nu}{h\dot{h}}f''_{33}+\frac{h\varepsilon_{33o}}{\dot{h}\langle u_3u_3\rangle_o}f_{\varepsilon 33}+2\frac{h\langle ps_{33}\rangle_o}{\dot{h}\langle u_3u_3\rangle_o}f_{ps}-2\frac{\langle pu_3\rangle_o}{\dot{h}\langle u_3u_3\rangle_o}f'_{pu}. \quad (3.11)$$

Combining the self-similarity groups from the moment equations produces

$$\langle u_3c\rangle_o=\dot{h}\frac{\langle cc\rangle_o}{C_o},\quad \langle u_3c\rangle_o=Ag\frac{h}{\dot{h}}\langle cc\rangle_o,\quad \langle u_3u_3\rangle_o=\frac{\dot{h}}{C_o}\langle u_3c\rangle_o,\quad \langle u_3c\rangle_o=\frac{\dot{h}}{Agh}\langle u_3u_3\rangle_o.$$

Combining the relationships with $\langle cc\rangle_o=C_o^2$ one obtains the following scalings for the second-order moments:

$$\langle cc\rangle_o=C_o^2,\quad \langle u_3c\rangle_o=\tfrac{1}{2}AgC_o^2t_0(\tau+1),\quad \langle u_3u_3\rangle_o=\tfrac{1}{4}(AgC_ot_0)^2(\tau+1)^2. \quad (3.12)$$

In the long time asymptotic regime one obtains

$$h(t)\sim\tfrac{1}{4}AgC_ot^2,\quad \langle cc\rangle_o=C_o^2,\quad \langle u_3c\rangle_o\sim\tfrac{1}{2}AgC_o^2t,\quad \langle u_3u_3\rangle_o\sim\tfrac{1}{4}(AgC_o)^2t^2. \quad (3.13)$$

The scalings obtained above, for the second moments, are independent of the conventional turbulence ansatz that the cascade rate is independent of viscosity (or diffusivity) and equal to the dissipation. That assumption does however affect how the dissipations scale. Using such an inviscid cascade notion, i.e. $\varepsilon=\varepsilon_o f_\varepsilon(\eta)$, the three dissipation rates scale as

$$\varepsilon_{co}=\frac{C_o^2}{t_0}\frac{2}{\tau+1},\quad \varepsilon_{3co}=AgC_o^2,\quad \varepsilon_{33o}=\tfrac{1}{2}(AgC_o)^2t_0(\tau+1). \quad (3.14)$$

The material mixing rate, ε_c, at the origin decays with time. The third-moment fluxes and the pressure strain scale as

$$\left.\begin{aligned}\langle u_3cc\rangle_o&=\tfrac{1}{2}AgC_o^3t_0(\tau+1),\qquad \langle u_3u_3c\rangle_o=\tfrac{1}{4}(AgC_o)^2C_ot_0^2(\tau+1)^2,\\ \langle u_3u_3u_3\rangle_o&=\tfrac{1}{8}(AgC_ot_0)^3(\tau+1)^3,\quad \langle ps_{33}\rangle_o=\tfrac{1}{2}(AgC_o)^2t_o^3(\tau+1)^3,\end{aligned}\right\} \quad (3.15)$$

and the pressure flux scales as $\langle pu_3\rangle_o=\frac{1}{8}(AgC_ot_0)^3(\tau+1)^3$.

It is seen that all turbulence moment quantities scale with some power of $(\tau+1)$. In as much as the mixing layer width scales as $h(t;C_o,t_0)=h_0(\tau+1)^2$ one sees a mathematical basis for the observation of Cook & Dimotakis (2001) regarding the utility of $h(t;C_o,t_0)$ as a progress variable. The Cook & Dimotakis (2001) simulations featured three different initial conditions. They observed that the computed $h(t;C_o,t_0)$ collapsed the data much better than time. This is due to the fact that $h=h(t;C_o,t_0)$ is a mapping between t and h with initial condition as a parameter. Thus the initial-condition-dependent mapping, $h=h(t;C_o,t_0)$, reflecting the short-time self-similarity solution is more useful as a progress variable than time for the initial condition studies of Cook & Dimotakis (2001).

4. Turbulence and mixing diagnostics: turbulence growth phase

There are several diagnostic quantities used in conventional descriptions of turbulence, see Tennekes & Lumley (1972), Pope (2000), that are useful to describe the turbulence physics. These are now investigated using the self-similar results. Comparisons with the direct numerical simulations are given in the next section.

As will be shown, the energy cascade length scale, $\ell = k^{3/2}/\varepsilon$, and the mixing layer width grow at the same rate. As a consequence the turbulence Reynolds number based on the layer width,

$$Re_o = \frac{k_o^{1/2} h}{\nu} = \frac{(AgC_o)^2}{8\nu}\, t_0^3(\tau+1)^3, \tag{4.1}$$

and the turbulence Reynolds number, $Re_t = k^2/\nu\varepsilon$, scale the same way. The Reynolds number based on the half-width has been chosen on the basis of the size of bubble/spike structures and, as will be seen, the energy-containing length scales of the motion.

The production–dissipation ratios are essential measures of the non-equilibrium nature of the flow. If the flow is self-similar the production–dissipation ratios are constant,

$$\left.\frac{P_c}{\varepsilon_c}\right|_o = \frac{\langle u_3 c\rangle_o C_o}{h\varepsilon_{co}} = \text{const}, \quad \left.\frac{P_{33}}{\varepsilon_{33}}\right|_o = \frac{Ag\langle u_3 c\rangle_o}{\varepsilon_{33o}} = \text{const}, \quad \left.\frac{P_{3c}}{\varepsilon_{3c}}\right|_o = \text{const}. \tag{4.2}$$

The definition of the last ratio can be ascertained from the $\langle u_3 c\rangle$ moment equation.

Four length scales are used to describe conventional homogeneous stationary turbulent flows. It is noted that RT turbulence is not stationary and the cascade rate and the viscous dissipation are not likely to be equal. An 'inviscid' energy-containing-range length scale scales as

$$\ell_o = \frac{k_o^{3/2}}{\varepsilon_o} = h_o(\tau+1)^2. \tag{4.3}$$

The energy-containing length scale is the mixing layer half-width. The result implies a proportionality to h even before the $\sim \frac{1}{4}AgC_o t^2$, asymptotic growth phase is attained. The approximation $k_o = \langle u_3 u_3\rangle_o$ has been made as the different components of the energy have the same scaling.

The Taylor microscales of the scalar and kinetic energy fields scale as

$$\lambda_{co}^2 = 3\mathscr{D}\frac{\langle cc\rangle_o}{\varepsilon_{co}} = \tfrac{3}{2}\mathscr{D}\, t_0\,(\tau+1), \qquad \lambda_o^2 = 10\,\nu\tfrac{k_o}{\varepsilon_o} = 5\nu\, t_0\,(\tau+1); \tag{4.4}$$

thus, asymptotically, $\lambda \sim \lambda_c \sim t^{1/2}$ and we have the usual viscous/diffusive scaling. Isotropy has been assumed and this does not make a difference as the different components of the energy have the same scaling. Computations verify the similar scaling (not size) of the Taylor microscales in any direction.

A small-scale length scale is defined from the viscous dissipation and the viscosity. Following the convention for stationary homogenous turbulence we call it the Kolmogorov microscale (Tennekes & Lumley 1972),

$$\eta_o = \left(\frac{\nu^3}{\varepsilon_o}\right)^{1/4} = \left(\frac{2\nu^3}{(AgC_o)^2 t_0(\tau+1)}\right)^{1/4}. \tag{4.5}$$

It is customary in turbulent flows to investigate the range of scales in the flow as reflected by the ratio η/ℓ. For the RT turbulence one has

$$\frac{\eta_o}{\ell_o} = 4\left(\frac{2\nu^3}{(AgC_o)^6}\right)^{1/4}\left(\frac{1}{t_0(\tau+1)}\right)^{9/4}. \tag{4.6}$$

Note that η_o/ℓ_o scales as $Re_t^{-3/4}$. The quantity ℓ_o/η_o can be thought of as the bandwidth of the turbulence spectrum. It grows like

$$\frac{\ell_o}{\eta_o} \sim \left(\frac{(AgC_o)^6}{2\nu^3}\right)^{1/4}(t_0(\tau+1))^{9/4} \tag{4.7}$$

for constant g. Thus in a doubling of time the bandwidth, or the number of active modes, grows by a factor of five. The bad news, from the view point of under-resolved numerical calculations, is that the smallest scales are getting smaller all the time. This is due to the ever increasing Reynolds number and the non-stationarity of the cascade as loosely approximated by ε.

If the flow is self-similar one has four turbulence length scales with three different temporal evolutions. This is not classical self-similarity analysis which requires all length scales to scale in the same way. The largest length scale is growing larger as t^2 and the smallest length scale decreasing as $t^{-1/4}$, and an intermediate scale charateristic of mixing structure as $\sim t^{1/2}$. The noteworthy result is that the Kolmogorov scalings $\eta_o/\ell_o \sim Re_t^{-3/4}(t)$ and $\lambda_o/\ell_o \sim Re_t^{-1/2}(t)$, thought to be a consequence of the constant stationary spectral flux through the inertial range, are attained.

The Taylor Reynolds number is used to discuss flow regimes,

$$Re_\lambda = \frac{\left(\frac{2}{3}k_o\right)^{1/2}\lambda_o}{\nu} = \sqrt{\frac{5}{6\nu}}\,AgC_o(t_0(\tau+1))^{3/2}. \tag{4.8}$$

The usual relationship $Re_\lambda \sim Re_t^{1/2}$ is seen. Related to the Taylor microscales is the relative time scale ratio of the two variance fields:

$$r(t) = \frac{k\varepsilon_c}{\frac{1}{2}\langle c^2\rangle\varepsilon} = \frac{3}{5}\frac{1}{Sc}\frac{\lambda^2}{\lambda_c^2} = \text{const.} \tag{4.9}$$

To characterize the mixedness of the flow it is usual to use the molecular mix fraction parameter, following Linden *et al.* (1994), Youngs (1994) and Wilson & Andrews (2002),

$$\theta_m = 1 - \frac{\langle\rho\rho\rangle}{\Delta\rho^2 f(1-f)}. \tag{4.10}$$

Using the Reynolds decomposition for the density, $\rho^* = \bar\rho + \rho$ and the definitions $\Delta\rho = \rho_c - \rho_h$, $\rho^* = \rho_a + \frac{1}{2}\Delta\rho\, c^*$, and $\rho_a = \frac{1}{2}(\rho_h + \rho_c)$ the first and second moments of the density and concentration are easily related:

$$\bar\rho = \tfrac{1}{2}(\rho_c + \rho_h) + \tfrac{1}{2}(\rho_c - \rho_h)C, \qquad \langle\rho\rho\rangle = \tfrac{1}{4}(\Delta\rho)^2\langle cc\rangle \tag{4.11}$$

since the density fluctuation is $\rho = \frac{1}{2}(\rho_c - \rho_h)\,c$, as can be verified from the Reynolds decomposition. The molecular mixing fraction parameter becomes, in these variables,

$$\theta_m = 1 - \frac{\langle cc\rangle}{(1-C)(1+C)} \tag{4.12}$$

which is constant if the flow is self-similar. Note that $0 \leqslant \theta_m \leqslant 1$: $\theta_m = 0$ corresponds to a state of no molecular mixing and $\theta_m = 1$ to full molecular mixing. It has not

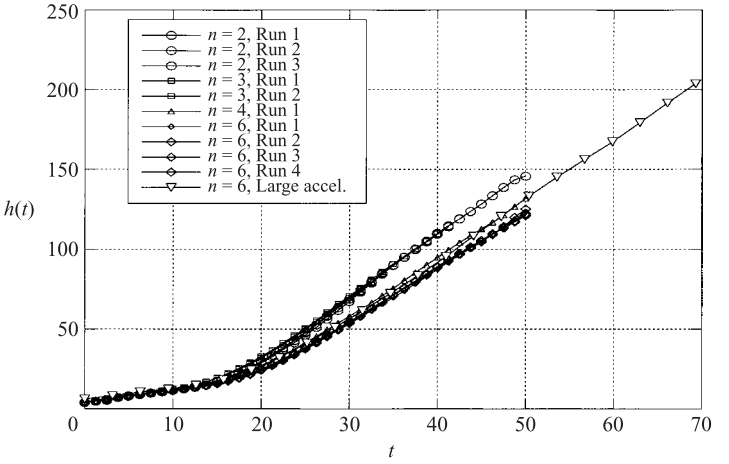

FIGURE 1. Mixing layer half-width, $h(t)$, in non-dimensional units.

been established that this corresponds to the percentage of mixed (at an intermediate composition) fluid. Using the results from the previous section, $\langle cc \rangle_o = \text{const}$, self-similarity indicates that the molecular mixing at $z = 0$ stays constant equal to what it was at the transition to the turbulence growth phase.

5. Numerical results: temporal scalings

The direct numerical simulation (DNS) results of the Rayleigh–Taylor flow are now reported and discussed in the context of the self-similar results. In this section the temporal scalings of the amplitude functions of the self-similar results at the origin or centreplane are investigated. In the following section the spatial scalings of the self-similar profiles are investigated.

5.1. *Development of the mixing layer*

Figure 1 shows the layer width as a function of non-dimensional time. As expected there are two different growth regimes, see also Cook & Dimotakis (2001). At non-dimensional time $t/t_c \approx 15$ the early-time $t^{1/2}$ diffusive growth phase ends and the turbulence growth phase, the subject of the self-similar analysis, begins. It should be pointed out that the late-time growth appears to be linear and this is due to the encroaching finite domain size. A fit to the mixing width data, shown below, does in fact show it to be quadratic.

The transition between growth laws is also reflected by the more rapid increase of the Reynolds numbers, see figures 2 and 3. The Reynolds numbers at transition to the turbulence growth phase are $Re \approx 125$ and $Re_{to} \approx 25$. Here the bulk or outer-scale Reynolds number is based on the total layer width, $2h$, thus $Re = 4\dot{h}h/\nu$. There is about a 20% difference in the mixing layer width and Reynolds number between the $n = 2$ and the $n = 6$ initial conditions. Apparently the larger the amount of energy in the low-wavenumbers the higher the growth rate. This point is discussed further below.

Snider & Andrews (1994) find that at about $Re \approx 1000$ their experimental flow approaches self-similarity as assessed by the mean concentration profile. Most of the present simulations are approaching $Re \approx 2000$ with the one long simulation reaching $Re \approx 3000$. Based on Snider & Andrews (1994) self-similar first-moment profiles are

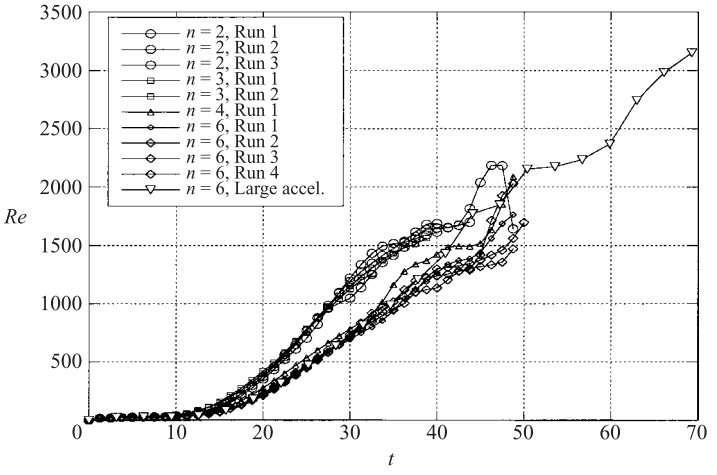

FIGURE 2. Bulk Reynolds number based on layer width: $Re = 4\dot{h}h/\nu$.

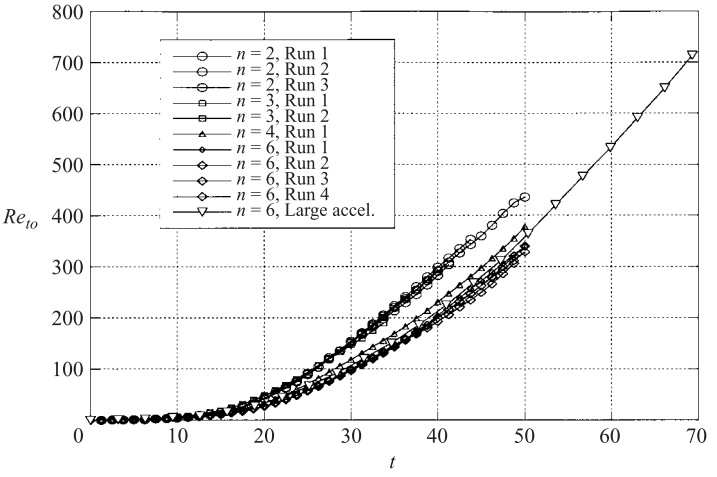

FIGURE 3. Turbulent Reynolds number at origin, $z = 0$: $Re_{to} = (\frac{2}{3}k_o)^{1/2}h(t)/\nu$.

expected to emerge well within the time period of the DNS. Using that criterion the simulations are well into the self-similar regime.

5.2. *Development of the nonlinearities*

In fully developed turbulence simulations it is customary to measure the duration of the flow in initial eddy turnover times. The diffusive $t^{1/2}$ regime ends at approximately $t/t_c = 15$ at which time the non-dimensional eddy turnover time, see figure 4, is about $(k_o/\varepsilon_o)_{t/t_c=15} \approx 5$. The eddy turnover time continues to increase, in a linear fashion, in accord with the self-similar results, by a factor of three. To translate the subsequent time evolution into a non-dimensional turbulent time scale one divides (k_o/ε_o) into the non-dimensional time. The length of time from $t/t_c = 15$ to $t/t_c = 50$ corresponds to about seven initial eddy turnover times. The long simulation goes to about eleven initial eddy turnover times. In typical DNS of homogenous turbulence this is ample time for most lower-moment statistics and those related to the cascade process (skewness) to approach stationarity. To this end we plot the derivative skewness as

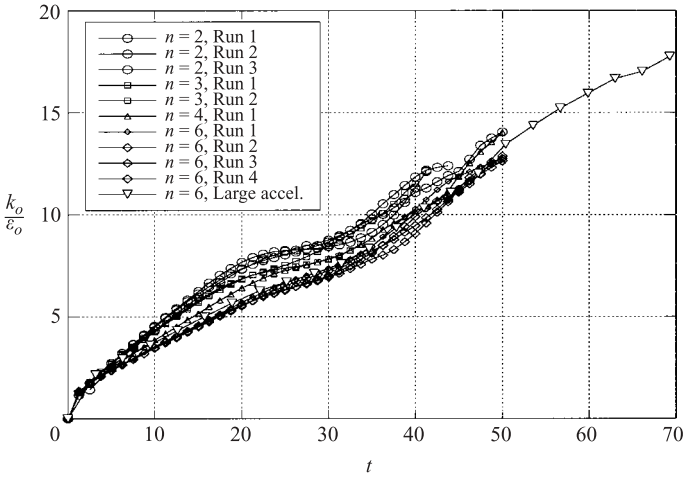

FIGURE 4. Non-dimensional eddy turnover time at the origin: k_o/ε_o.

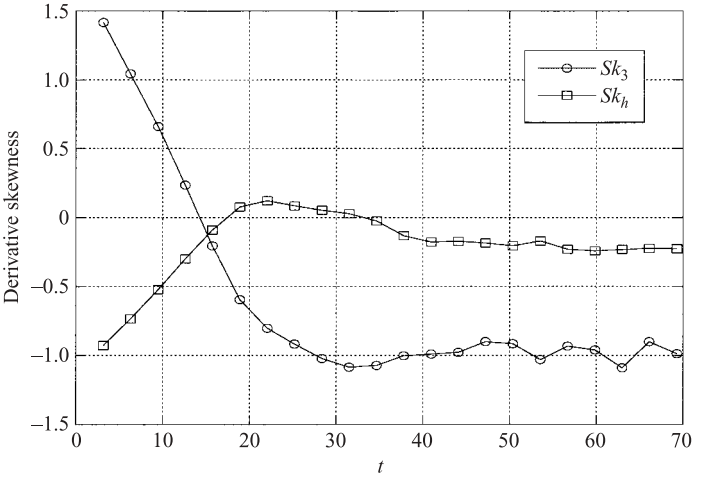

FIGURE 5. Derivative skewnesses at $z = 0$.

an indicator of the enstrophy production by straining. Figure 5 shows the derivative skewnesses $Sk_\alpha = \langle u_\alpha, {}^3_\alpha \rangle / \langle u_\alpha^2 \rangle^{3/2}$ in the two directions, at the origin, for the long $n = 6$ run. They seem to have equilibrated after about $t/t_c = 30$ indicating the establishment of the nonlinear cascade process. This a crucial fact that helps justify the application of the low-Reynolds-number simulations to higher-Reynolds-number situations. For fully developed isotropic turbulence $Sk = -0.5$.

Higher-order moments might reach self-similarity later. An assessment of the development of the nonlinearities responsible for the cascade in comparison to the dissipation is useful with regard to the applicability of the self-similar moment analysis to the simulations (and vice versa). Figure 6 compares the nonlinear cubic term to the linear dissipation,

$$\frac{\langle u_3 u_3 u_3 \rangle, {}_{3o}}{\varepsilon_o}. \tag{5.1}$$

Again differentiation of such a small sample size makes the plot noisy at later times. Nonetheless these ratios become of order one (and larger) at the transition

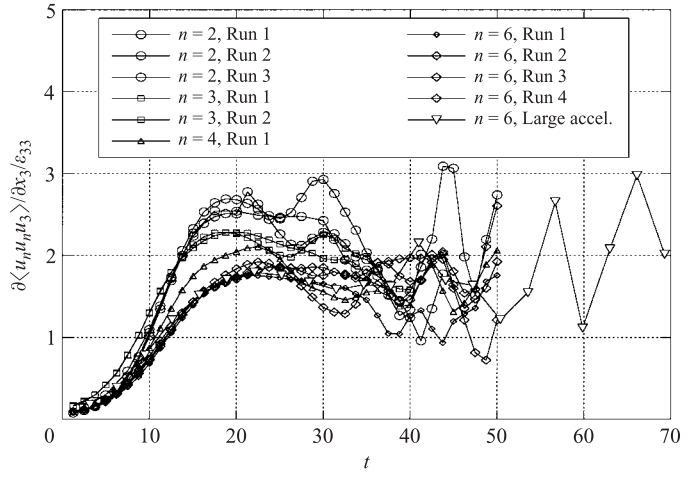

FIGURE 6. Establishment of nonlinearity: divergence of vertical flux of energy normalized by dissipation at origin, $\langle u_3 u_j u_j \rangle_{,o3}/\varepsilon_o$.

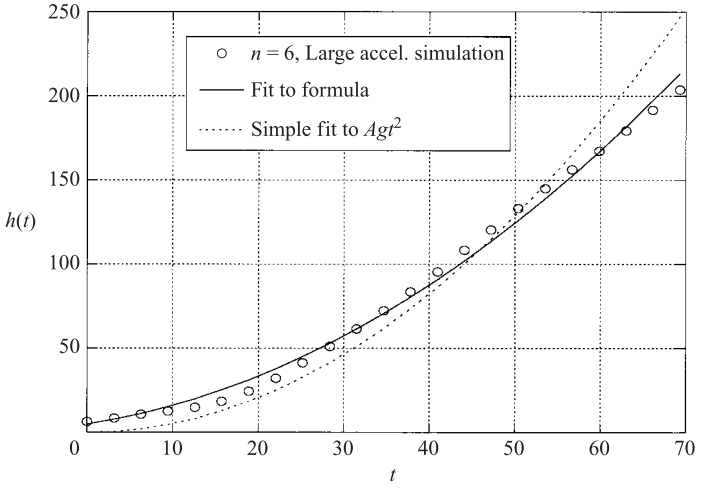

FIGURE 7. Least-mean-square fits to the DNS data: simple fit and equation (3.10).

time, $t/t_c \approx 15$, indicating the predominance of nonlinear terms and a subsequent nonlinear saturation. The above facts suggest the attainment of a turbulence growth phase in which the balance of terms is unlikely to be substantially different from longer simulations with higher Reynolds numbers.

5.3. *Mixing layer width: initial condition dependence and* α

One of the salient features of the self-similar analysis is the dependence of the asymptotic growth rate on the initial conditions at transition of C_o, h_0 or equivalently t_0, h_0 through

$$\frac{h_0}{t_0^2} = \frac{AgC_o}{4} \tag{5.2}$$

appearing in the virtual origin form of the mixing layer width, (3.10). Figure 7 shows two least-mean-square fits to the DNS data for the long $n = 6$ run. The solid line is the least-mean-square fit using the self-similar result, (3.10) for which $h_0/Agt_0^2 = \alpha = 0.040$.

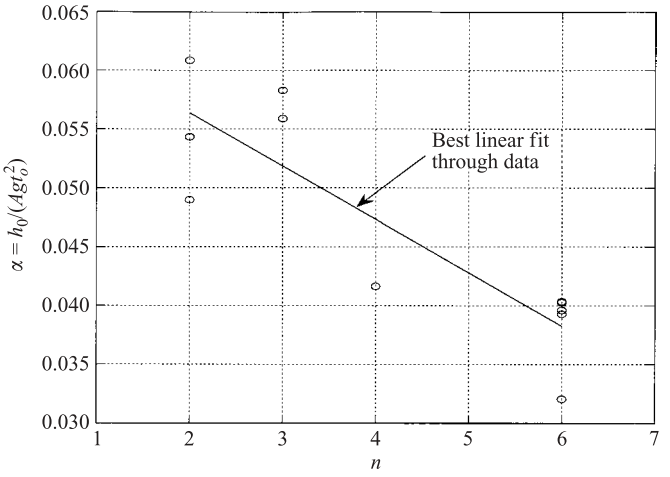

FIGURE 8. The α coefficient as a function of the low-wavenumber exponent.

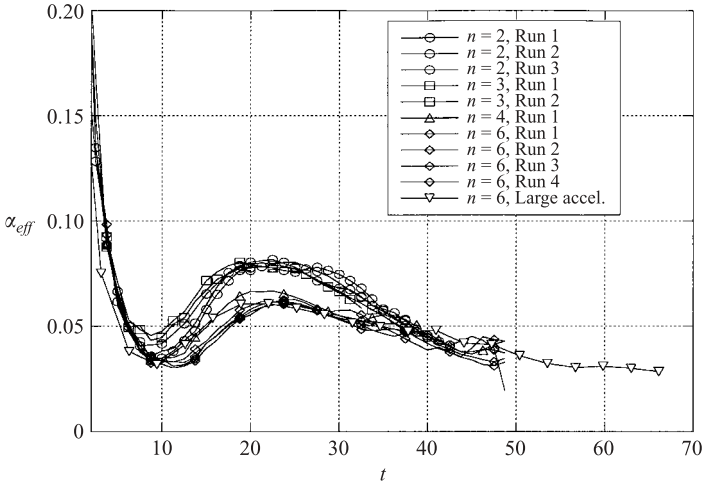

FIGURE 9. Instantaneous or effective α, (3.8).

The dashed line is the $\alpha g t^2$ fit for which $\alpha = 0.0727$. There is almost a factor of two difference in the α. It is clear that the fit (3.10), also a single parameter fit, which accounts for the virtual origin in a mathematically consistent way, is more accurate over a larger range.

A plot of the different α values as a function of the low-wavenumber exponent, figure 8, indicates a statistically significant trend of smaller α with increasing n. For the 11 simulations the asymptotic α varies by a factor of about two, $0.033 < \alpha < 0.60$. The stochastic nature of the initial conditions must be kept in mind when interpreting the data. Recall that the initial spectra peak at the same wavenumber and that there are no deterministic low-wavenumber components, which is expected to have a sizable influence on the growth given the observations of Linden *et al.* (1994) and Dalziel *et al.* (1999).

From (3.8) the effective α is given in figure 9. It is seen that α, while in the range of many measured and computed values, is not constant in time and decays in accord with the self-similar result.

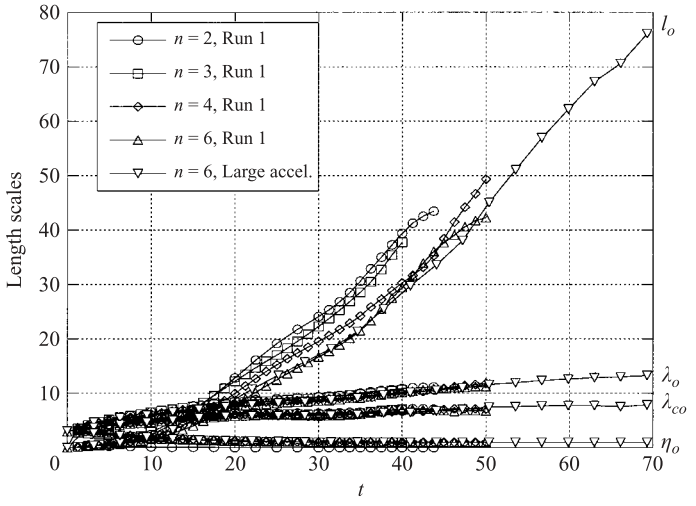

FIGURE 10. Turbulence length scales at $z = 0$: energy-containing length scale, ℓ, the Taylor microscales, λ, λ_c, the Kolmogorov length scale, η.

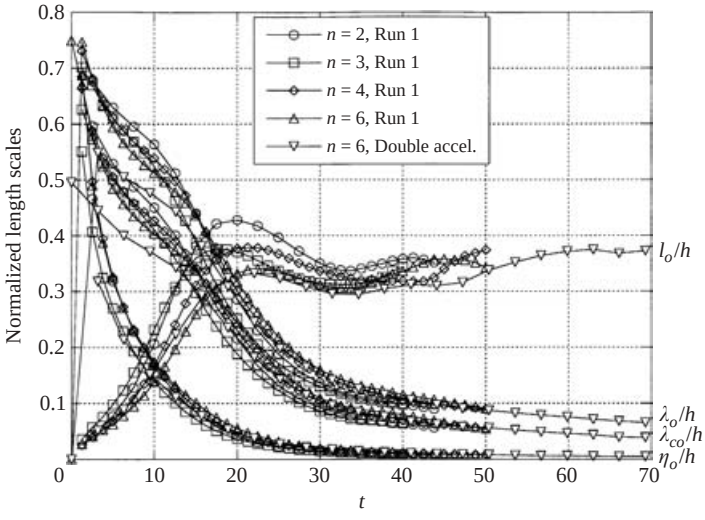

FIGURE 11. Turbulence length scales at $z = 0$ normalized by $h(t; C_o, h_0)$.

5.4. *Temporal self-similarity of turbulence length scales*

The four length scales characterizing the mixing layer turbulence $\ell_o, \lambda_o, \lambda_{co}, \eta_o$ are given in figure 10. The energy-containing length scale is smaller than the Taylor microscale until the diffusive phase ends at $t/t_c \approx 15$, $Re \approx 125$, after which time it begins a t^2 growth while the microscale grows as $t^{1/2}$. The four length scales $\ell_o, \lambda_o, \lambda_{co}, \eta_o$ normalized by $h(t; C_o, h_0)$ are shown in figure 11. If the flow exhibited a conventional length scale self-similarity the length scales so normalized would be constant. Only the outer energy-containing range turbulence length scale shows scale similarity with the mixing layer width (as is consistent with the self-similar result). In figure 12 the turbulence length scales normalized according to the self-similarity

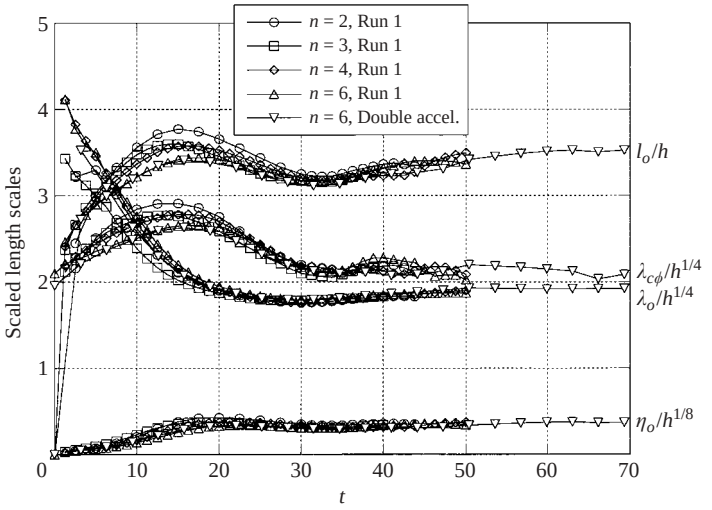

FIGURE 12. Turbulence length scales at $z = 0$ normalized by the self-similar scaling.

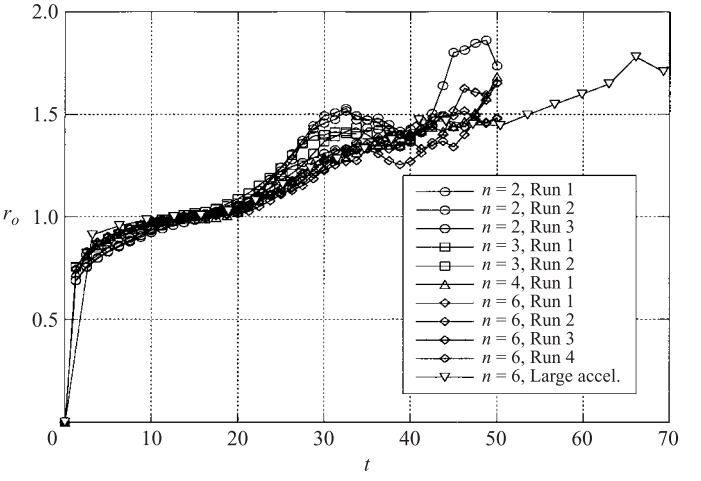

FIGURE 13. The turbulence time scale ratio.

results

$$\ell_o\, h^{-1}, \quad \lambda_o\, h^{-1/4}, \quad \lambda_{co}\, h^{-1/4}, \quad \eta_o h^{1/8}, \tag{5.3}$$

are presented. Scalings consistent with self-similarity are achieved at about three initial eddy turnover times after the inception of the turbulence growth phase at which time $Re > 700$–1000 and $Re_{to} > 100$–150. This coincides with the establishment of the cascade as measured by the constancy of the derivative skewnesses. The turbulence length scales $\ell_o, \lambda_o, \lambda_{co}, \eta_o$ are arrived at by dimensional reasoning using the viscous dissipation and not the assumption of a constant-flux inertial range as done by Kolmogorov. Nonetheless, and despite the non-stationarity and the cascade to larger length scales of RT turbulence, the traditional Kolmogorov scalings, $\eta_o/\ell_o \sim R_t^{-3/4}(t)$, $\lambda_o/\ell_o \sim R_t^{-1/2}(t)$, as predicted by the self-similar analysis are clearly seen in the DNS.

The time scale ratio (4.9) at the origin is given in figure 13. The time scale ratio is assumed constant in many turbulence closures as a closure for the scalar dissipation.

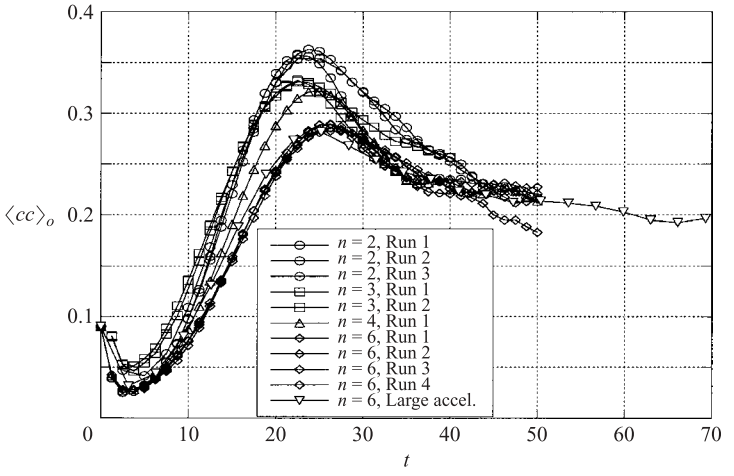

FIGURE 14. Non-dimensional scalar variance, $\langle cc\rangle_o$.

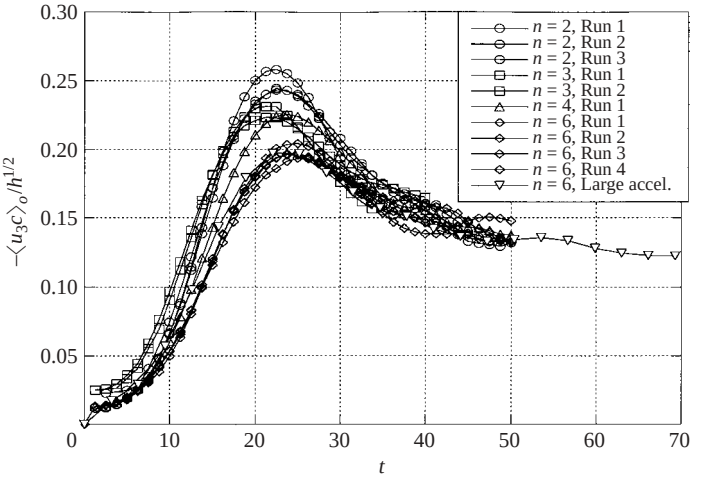

FIGURE 15. Non-dimensional scalar flux, $\langle u_3 c\rangle_o$, normalized by self-similar scaling.

The DNS shows a factor two increase during the simulation. This is not consistent with self-similarity. The assumed constancy of $r(t)$ in turbulence models, in the face of the fact of its factor of two change, will result in substantial error in the prediction of the scalar variance and the mixing rate. The time scale ratio indicates no tendency to become constant.

5.5. *Temporal self-similarity of the second-order moments*

As discussed above Cook & Dimotakis (2001) have indicated the success of $h(t\,; C_o, h_0)$ as a progress variable. Here $h = h(t\,; C_o, h_0)$ is used to test for self-similarity by normalizing the dependent variables by the appropriate power of $h(t\,; C_o, h_0)$ according to the self-similarity results. The three normalized second-order moments,

$$\langle cc\rangle_o, \quad \langle u_3 c\rangle_o h^{-1/2}(t\,; C_o, h_0), \quad \langle u_3 u_3\rangle_o h^{-1}(t\,; C_o, h_0)\,, \tag{5.4}$$

are given in figures 14, 15 and 16. If the flow is self-similar, at any time during the turbulence growth phase, even before the initial condition dependence (of the

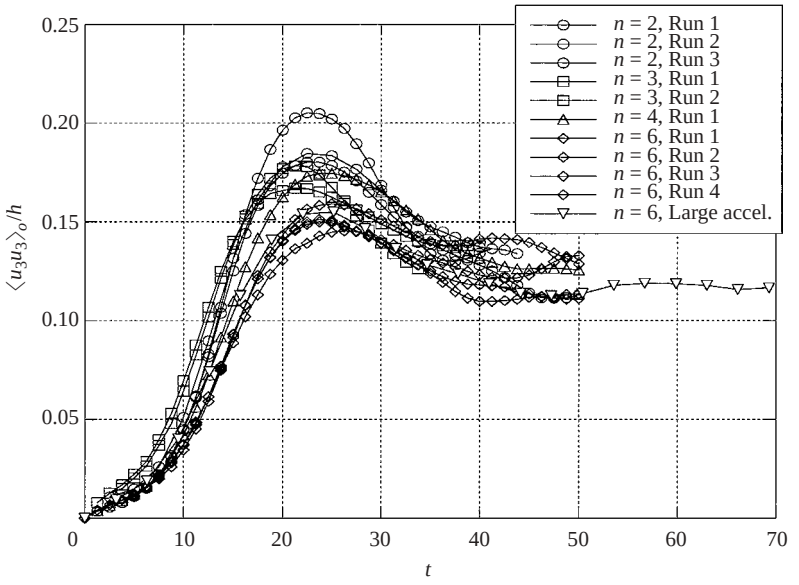

FIGURE 16. Non-dimensional variance, $\langle u_3 u_3 \rangle_o$, normalized by self-similar scaling.

turbulence growth phase) has vanished, the second-order moments so normalized will be constant. Several of the simulations indicate the inception of an approximately constant regime at about $Re \approx 1500$–1800, after about seven eddy turnover times. This is vindicated by the longer simulation.

RT turbulence is expected to be highly anisotropic. A non-dimensional Reynolds stress anisotropy tensor devised by Lumley (1978) is used to describe the Reynolds stresses,

$$b_{ij} = \frac{\langle u_i u_j \rangle}{\langle u_k u_k \rangle} - \tfrac{1}{3}\delta_{ij} \tag{5.5}$$

where $\langle u_k u_k \rangle = 2k$ is twice the kinetic energy of the turbulence. For those not familiar with the use of the anisotropy tensor the following facts are noted. The anisotropy tensor b_{ij} is bounded: $-\frac{1}{3} \leqslant b_{ij} \leqslant \frac{2}{3}$. The limit $-\frac{1}{3}$ corresponds to no energy in the (α, α) component of b_{ij}. The value $b_{\alpha\alpha} = \frac{2}{3}$ corresponds to all the energy in the α component, i.e. a one-dimensional flow. The off-diagonal terms of the anisotropy tensor are zero indicating that there are no turbulent shear stresses. Thus, in principle, an eddy diffusivity such as those used in standard k–ε models cannot predict such a flow. It is in fact the mean concentration gradient that drives RT turbulence. The b_{33} component of the anisotropy tensor is shown in figure 17. It indicates how much of the total energy is in the vertical component (at the origin). At early time, when $b_{33} \approx 0.6$, almost 93% of the energy is in the vertical component. At late time about 66% of the energy is in the vertical component. Self-similarity requires $b_{33} = \text{const}$ and this is only slowly approached as the pressure–strain redistributes energy from the vertical to horizontal components of the velocity field for $t/t_c = 40$a.

The bulk mixing parameter at the origin is shown in figure 18. It starts at about 1 reflecting the molecular mix of the initial concentration. As the fluids from above and below interpenetrate each other, stirring but not yet mixing, θ_m drops. Then θ_m begins to rise after the transition to the turbulence growth phase and the concommitant

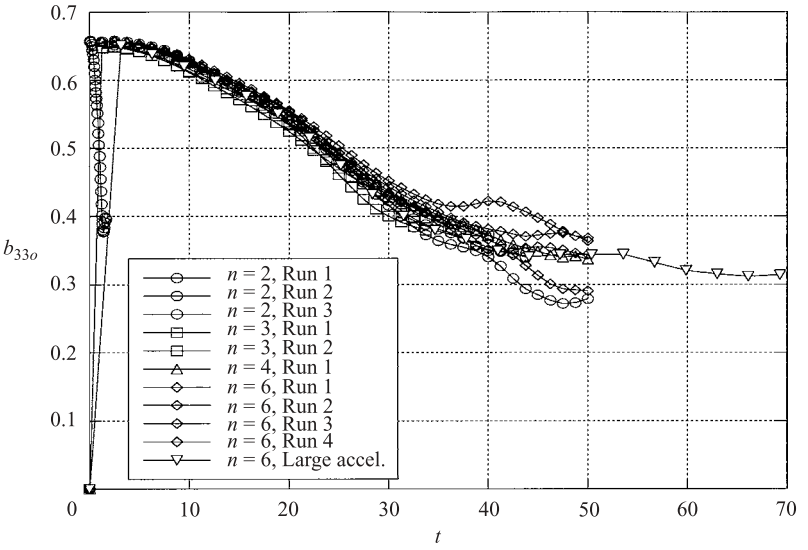

FIGURE 17. Vertical component of the anisotropy tensor, b_{33o}.

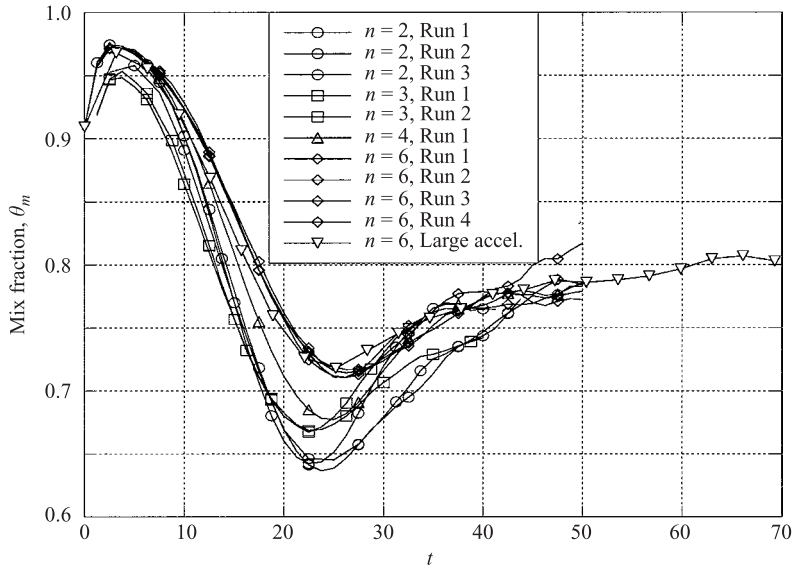

FIGURE 18. Bulk mixing parameter, θ_m, at the origin.

more efficient mixing. In any event at no time is there any indication of an approach to a 'fully mixed', $\theta_m = 1$, state.

5.6. *Temporal self-similarity of mixing rate and dissipations*

The mixing rate and the two normalized dissipations

$$\varepsilon_{co} h^{1/2}, \quad \varepsilon_{33o} h^{-1/2}, \quad \varepsilon_{3co}, \tag{5.6}$$

are given in figures 19, 20, 21. Of the three dissipations that of the scalar appears to be approaching a result consistent with self-similarity. It should be mentioned that

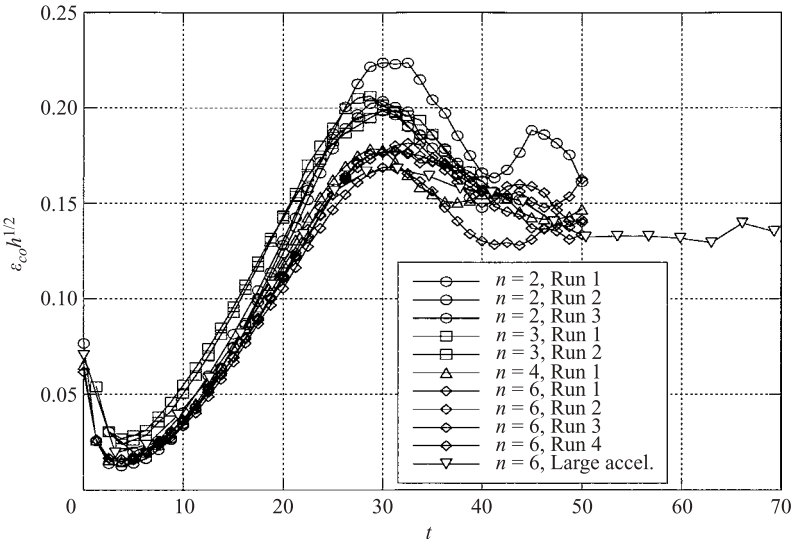

FIGURE 19. Scalar dissipation at the origin, ε_{co}, normalized by the self-similar scaling.

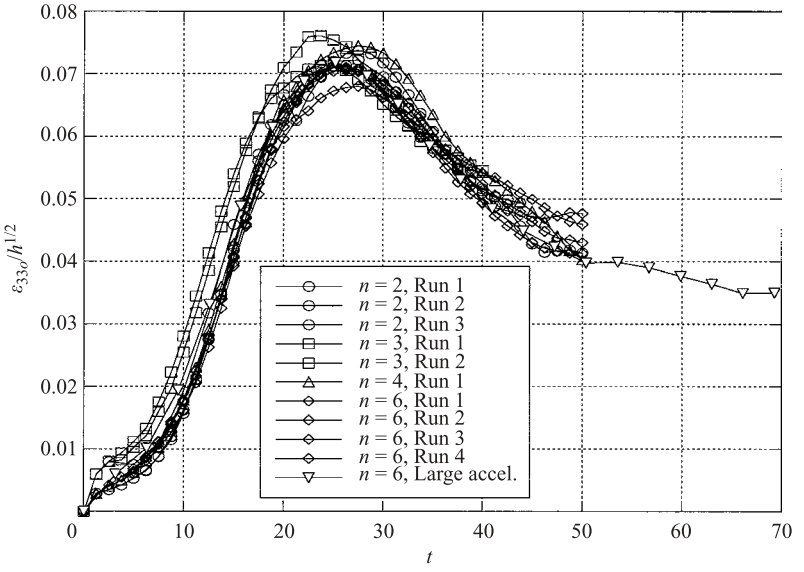

FIGURE 20. Vertical component of dissipation, ε_{33o}, normalized by the self-similar scaling.

the self-similar forms assumed for the dissipations involve a cascade rate assumption which implies high Reynolds number and stationarity. As a consequence the extent of the lack of self-similarity of the dissipation may be due to either low-Reynolds-number effects or non-stationarity or the lack of self-similarity. The cascade assumption does not effect the variances, the flux or the mixing width self-similarity.

The self-similar analysis indicates that the production dissipation ratios, shown in figures 22, 23, are constant. The production–dissipation ratios for the variances appear to behave very consistenly with the self-similar predictions. Near the end of the simulations the production–dissipation ratio for the scalar variance, having peaked

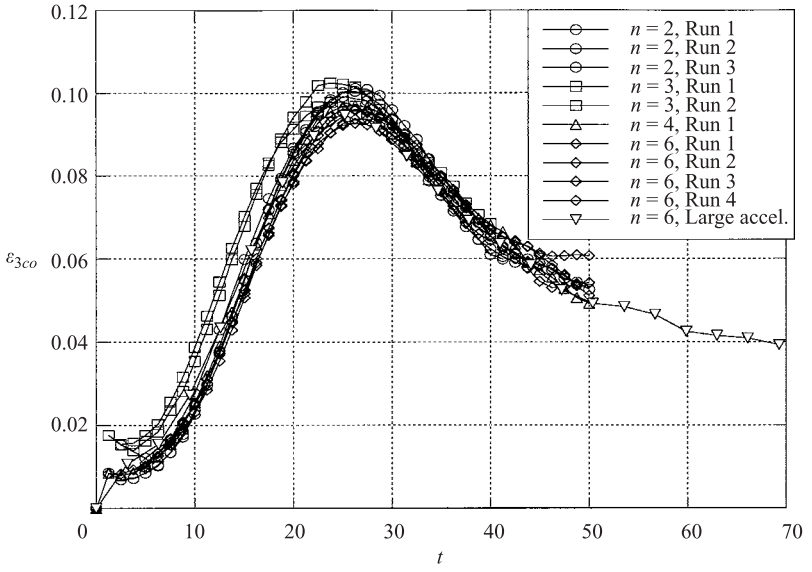

FIGURE 21. Scalar flux dissipation, ε_{3co}, normalized by the self-similar scaling.

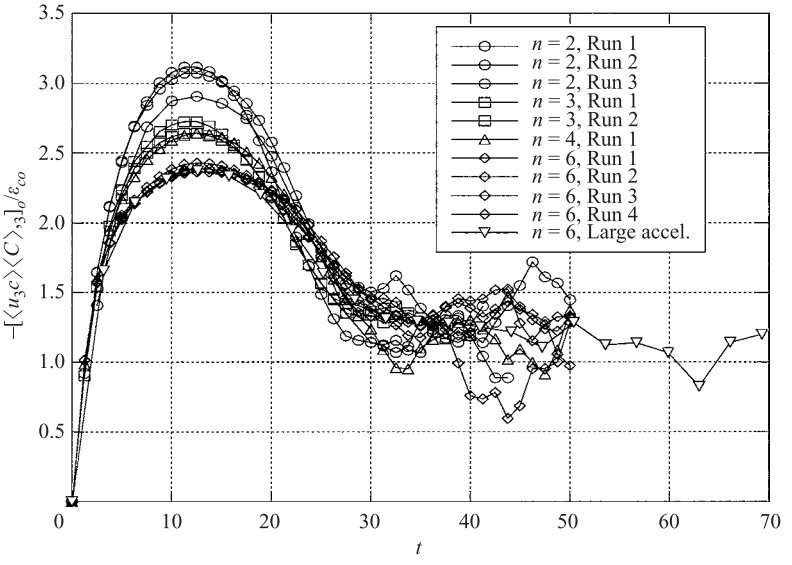

FIGURE 22. Scalar production–dissipation ratio at $z = 0$.

near the transition to the turbulence growth phase, is only modestly larger than unity. The production–dissipation ratio for the energy is surprisingly large indicating a highly non-equilibrium situation in which the energy grows rapidly, as seen in the increase in Reynolds number, with little dissipated locally. The large value, in comparison to the scalar production–dissipation, is likely to be due to the fact that the velocity field does not start with the small length scales that are part of the initial condition on the scalar field. The production–dissipation ratio for the scalar flux (not shown) is not in accord with the self-similar results.

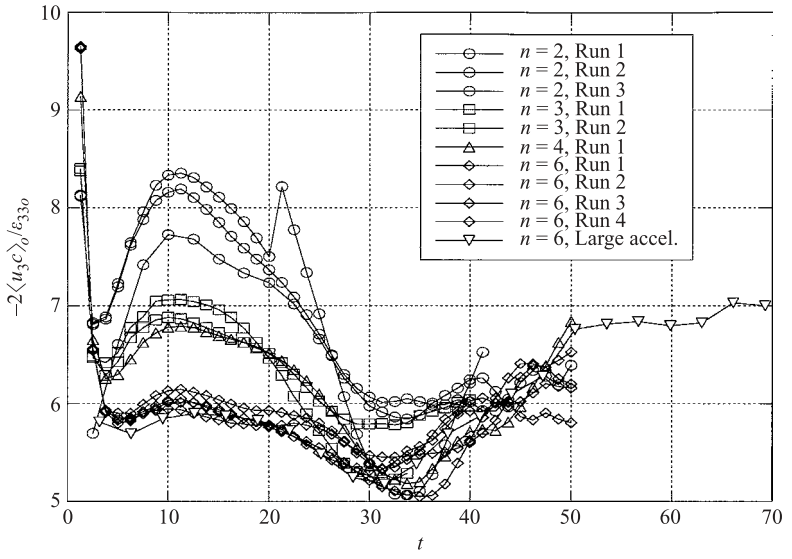

FIGURE 23. Energy production–dissipation ratio at the origin.

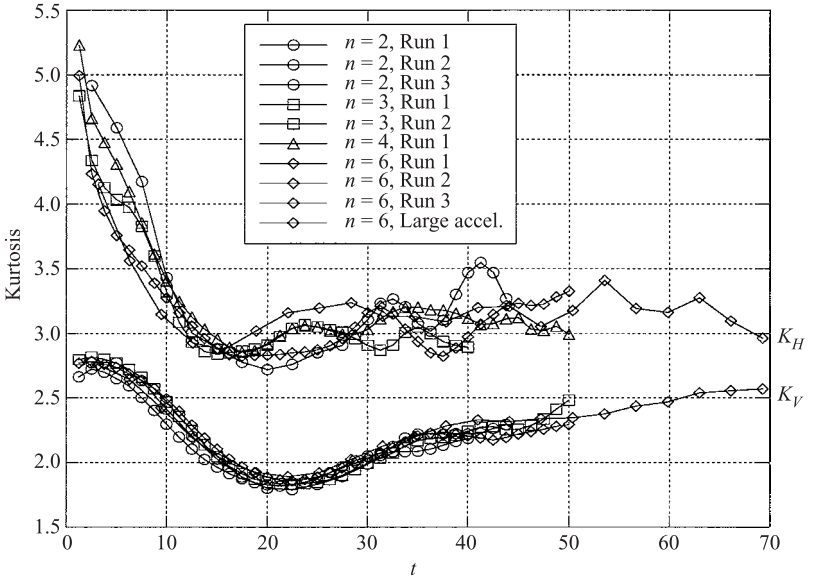

FIGURE 24. Velocity kurtosis at $z = 0$.

5.7. *Temporal self-similarity of higher-order moments*

The triple moments and skewnesses will be zero at the origin (due to symmetry). The kurtoses, figures 24, 25 will not be zero at the origin. Self-similarity requires that

$$K_c = \frac{\langle c^4\rangle}{\langle c^2\rangle^2}, \qquad K_\alpha = \frac{\langle u_\alpha^4\rangle}{\langle u_\alpha^2\rangle^2} \tag{5.7}$$

(no sum on α) be constant. The kurtosis for the velocity field in the homogeneous directions is seen to approach that of a Gaussian field, figure 24. The kurtosis of the

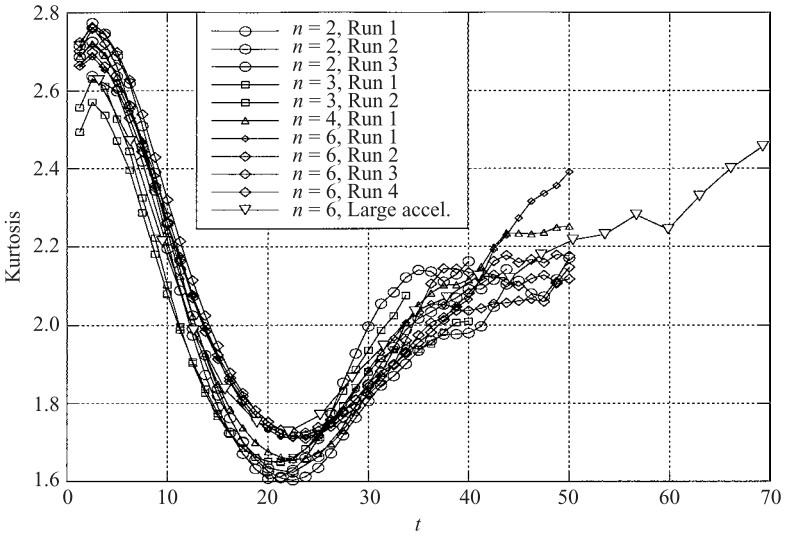

FIGURE 25. Scalar kurtosis at $z = 0$.

vertical velocity field, due to the driving force, is smaller indicating a more compact probability density function (p.d.f.).

The kurtosis for the scalar field is shown in figure 25. The scalar field is initialized with some mixing set up by the initial concentration spectrum smeared to resemble a diffusion layer. As the pure fluids interpenetrate from above and below the origin stirring but not mixing occurs and the kurtosis drops. For no molecular mixing $K_c = 1$. As diffusion sets in the kurtosis begins to increase to levels more characteristic of molecular mixing. It is useful to keep in mind that $K_c = 1.8$ corresponds to a uniform p.d.f. in which the probability of finding any arbitrary concentration between [0, 1] is the same. The kurtosis of the scalar field does not approach a constant, during the time of the DNS, as would be consistent with the self-similar analysis.

5.8. *Summary of § 5 numerical results*

Various quantities suggesting the progress of the flow indicate that the nonlinearities are fully developed. The DNS results indicate that the most important second-order moments, $\langle cc \rangle_o$, $\langle u_3 c \rangle_o$, and $\langle u_3 u_3 \rangle_o$, begin to scale consistently with the self-similar results after about five initial eddy turnovers and $Re > 1500$ and $Re_{to} > 250$. The two variances agree more closely with the self-similar results than the scalar flux. The dissipation and production–dissipation ratios for the variances, $\langle cc \rangle_o$ and $\langle u_3 u_3 \rangle_o$, exhibit a scaling only modestly consistent with the self-similar results after about five initial eddy turnovers. The quantities that do clearly scale as predicted by the self-similar analysis are the four turbulence length scales: ℓ_o, λ_o, λ_{co} and η_o. In the DNS this occurs within about three initial eddy turnover times of the inception of the turbulence growth phase and $Re > 700$–1000 and $Re_{to} > 100$–150 and coincides with the establishment of the derivative skewness and the saturation of the enstrophy production.

There is a modest 20% difference in the mixing layer width and Reynolds number between the $n = 2$ and the $n = 6$ initial conditions. Apparently the larger the amount of energy in the low wavenumbers the higher the growth rate. This is consistent with the results of Cook & Dimotakis (2001) as can be concluded from their figures 2, 6 and 8. Cook & Dimotakis (2001) concluded that the relative location of the peak of the initial spectra explained the different growth rate. In the present simulations the

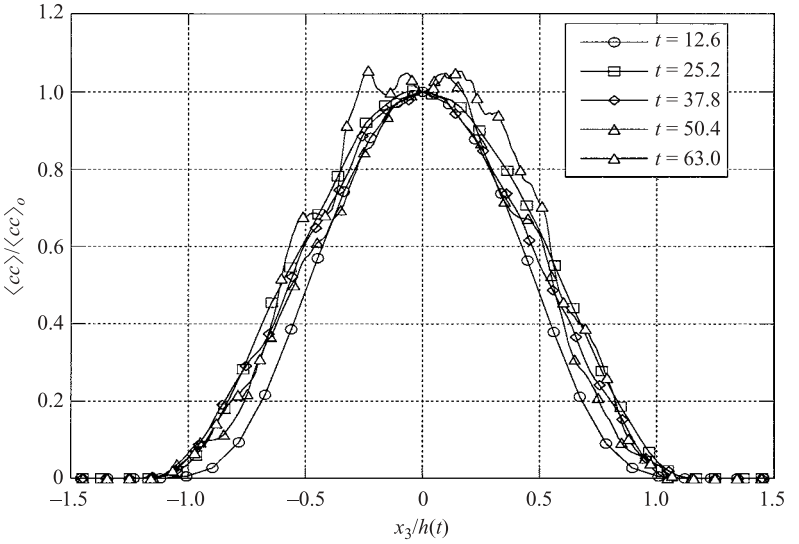

FIGURE 26. Normalized $\langle cc\rangle$ profiles at selected times.

spectral peaks of all the simulations are the same. It is not possible conclude whether the low-wavenumber exponent or the relative spectral peak effect is more important.

6. Numerical results: spatial profiles

Evaluating the self-similarity of the moment quantities at the origin is a test of self-similarity of the temporal amplitude functions. The core region, after transition, is primarily a fully developed quasi-homogeneous part of the flow for which self-similar ansatzen might be expected to work. It is however the edge regions that are crucial to understanding the mixing layer entrainment. In this section the profiles of various turbulence quantities are plotted as a function of the normalized spatial coordinate, $x_3/h(t; C_o, h_0)$, across the layer at selected times. The edge, where $x_3/h(t) = 1$, is defined as where the mean concentration level is 95% of the far field. To investigate the spatial aspect of self-similarity – independent of the temporal nature – the profiles are normalized by their current centreline values. All the profiles shown are from the long $n = 6$ run. It is pointed out that there are no predictions from the self-similar analysis for the spatial profiles; this would require solution of the unclosed set of self-similar second-moment equations. The interest is in establishing the utility of the spatial self-similar ansatz.

6.1. *Spatial self-similarity of second-order moments*

The three second-order moments normalized by their temporally varying centreline value $\langle cc\rangle_o, \langle u_3u_3\rangle_o, \langle u_3c\rangle_o$ are shown in figures 26, 27, and 28. Having factored out the temporal self-similarity it is seen that the profiles collapse. Related non-dimensional measures, the anisotropy tensor, b_{33}, and the mix parameter, θ_m, are shown in figures 29 and 30. Only at late time do these begin to behave in accordance with the self-similarity. The b_{33} decreases at the edges, and the turbulence is more isotropic in the edge regions than it is in the core due to the anisotropy of the production which is set by the mean concentration gradient which is largest in the core of the layer. The anisotropy continues to decrease towards the edge region of the box because the no flux condition requires $b_{33} = -\frac{1}{3}$.

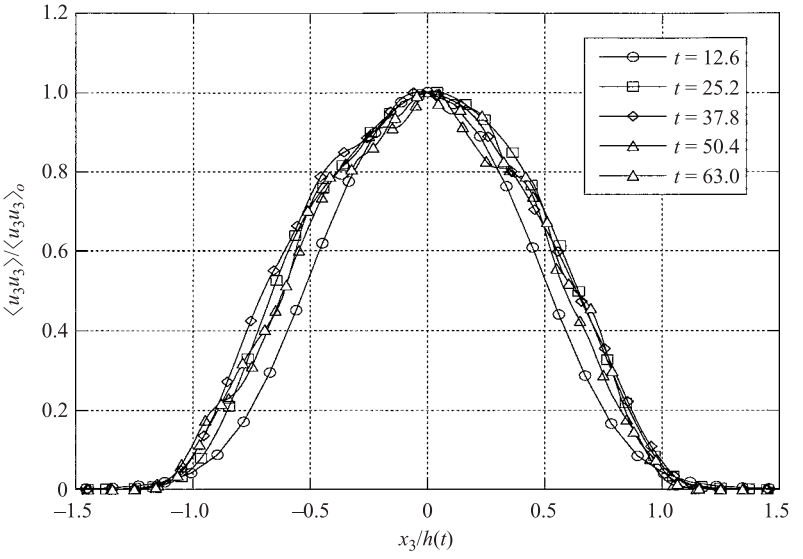

FIGURE 27. Normalized $\langle u_3u_3\rangle$ profiles at selected times.

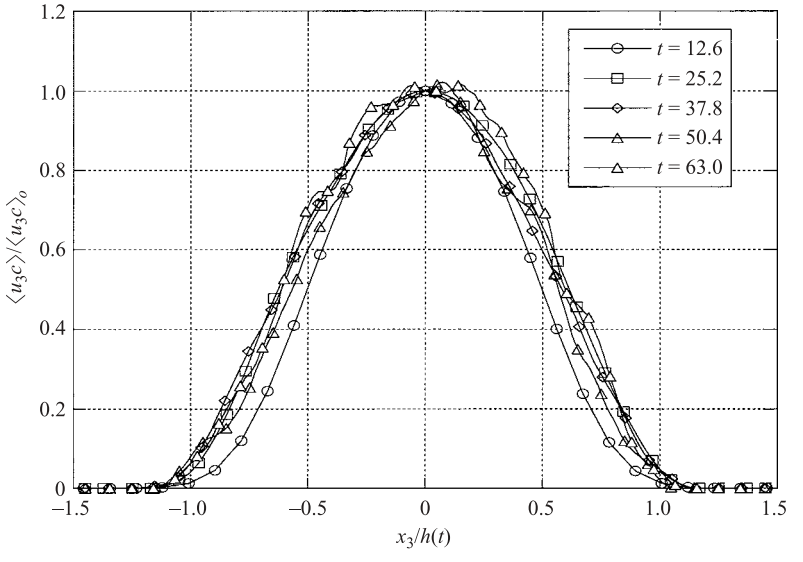

FIGURE 28. Normalized $\langle u_3c\rangle$ profiles at selected times.

The mixing parameter behaves similarly to the bulk mixing parameter given in Cook & Dimotakis (2001). It is high at the beginning of the flow, dips to a lower value, and then equilibrates to about $\theta_m \approx 0.8$ throughout much of the core region. It does not appear to approach behaviour consistent with self-similarity until about five initial eddy turnover times at $Re \approx 1200$–1500. The correlation coefficient, figure 31, is given by

$$\rho_{3c} = \frac{\langle u_3c\rangle_o}{\langle cc\rangle_o^{1/2}\langle u_3u_3\rangle_o^{1/2}}. \tag{6.1}$$

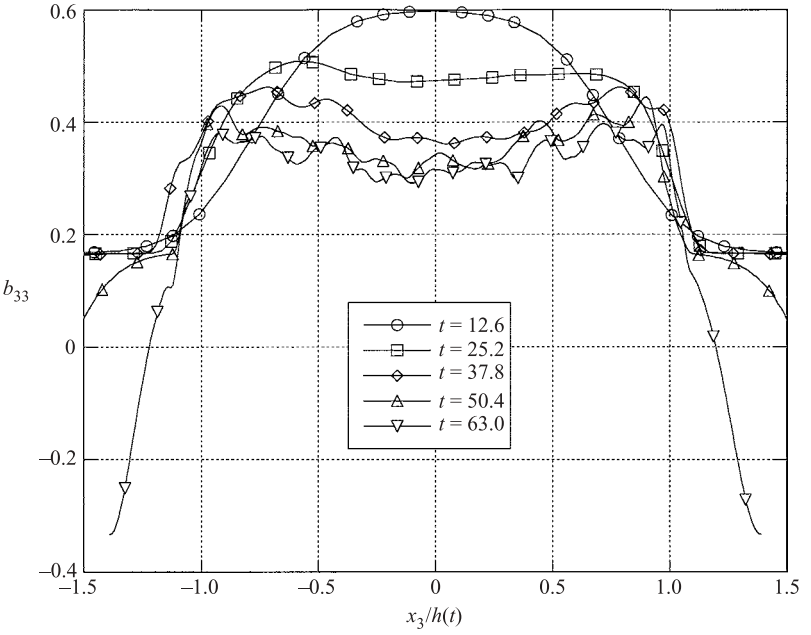

FIGURE 29. Profiles of b_{33}.

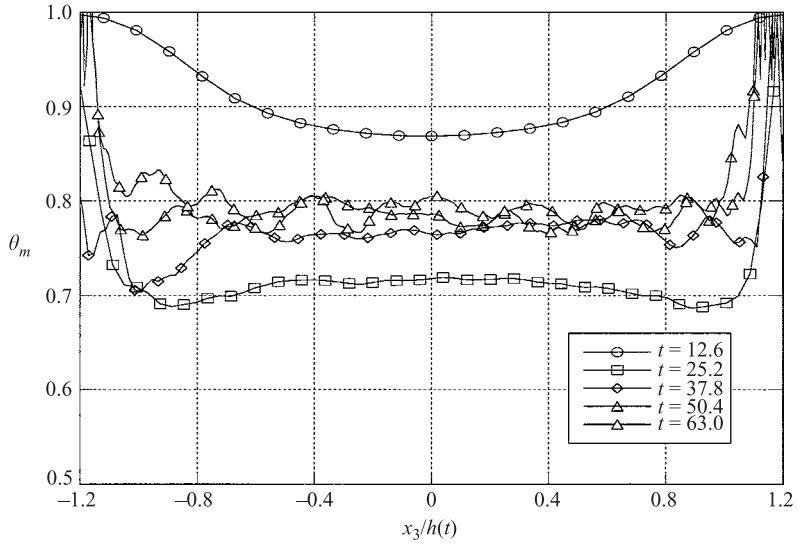

FIGURE 30. The bulk mixing parameter profiles.

It is a constant (in time) if the flow is self-similar. The approximate spatial constancy of ρ_{3c} across most of the layer is noteworthy.

6.2. *Production–dissipation profiles*

The production–dissipation ratios, (4.2), are useful measures of the non-equilibrium nature of the flow. They are shown in figures 32 and 33. Figure 32 is noisy at late time due to differentiation of the mean concentration. The production of the scalar fluctuations takes place in the central 75% of the mixing layer. Near the

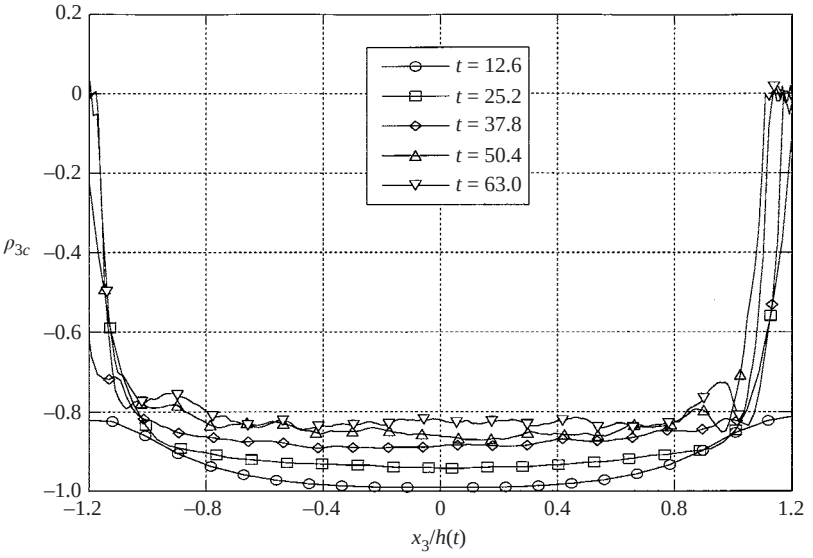

FIGURE 31. The scalar flux correlation coefficient profiles.

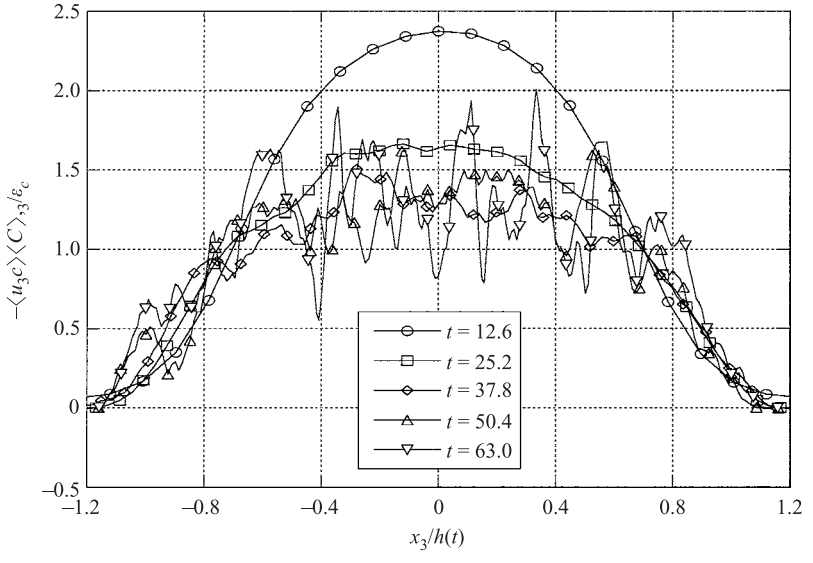

FIGURE 32. Scalar variance production–dissipation profile.

edges the dissipation dominates production. In contradistinction the production of the turbulent kinetic energy exceeds dissipation by a factor of four throughout most of the mixing layer indicating the highly non-equilibrium nature of a RT mixing layer and a continual increase of the turbulence Reynolds number and a cascade of energy to ever increasing scale. One might speculate if this is due to the cascade of energy to larger length scales mitigating the cascade to smaller lengths thus decreasing viscous dissipation. It is noted that that most flows in engineering applications have production–dissipation ratios not far from unity.

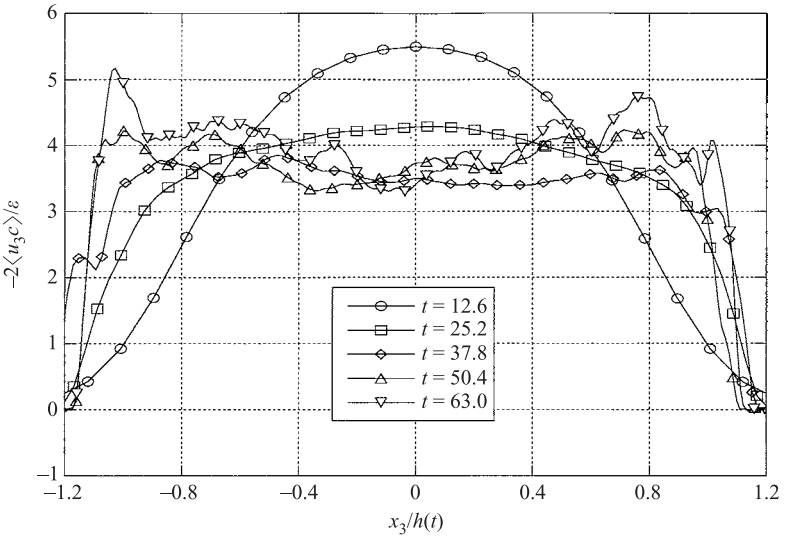

FIGURE 33. Turbulent kinetic energy production–dissipation profile.

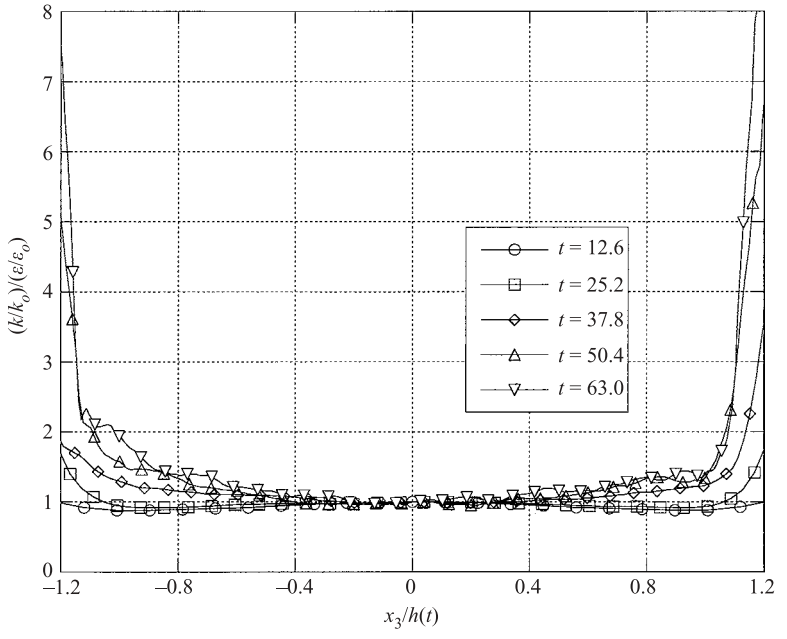

FIGURE 34. The eddy turnover time, k/ε, profile.

6.3. *Spatial self-similarity of length and time scales*

The eddy turnover time and the time scale ratio profiles are shown in figures 34 and 35. The apparent singular behaviour at the edges poses a problem for single-point closures and gradient transport type models. The local energy-containing turbulence length scale ℓ and the isotropic forms of the Taylor microscales are shown figures 36, 37 and 38.

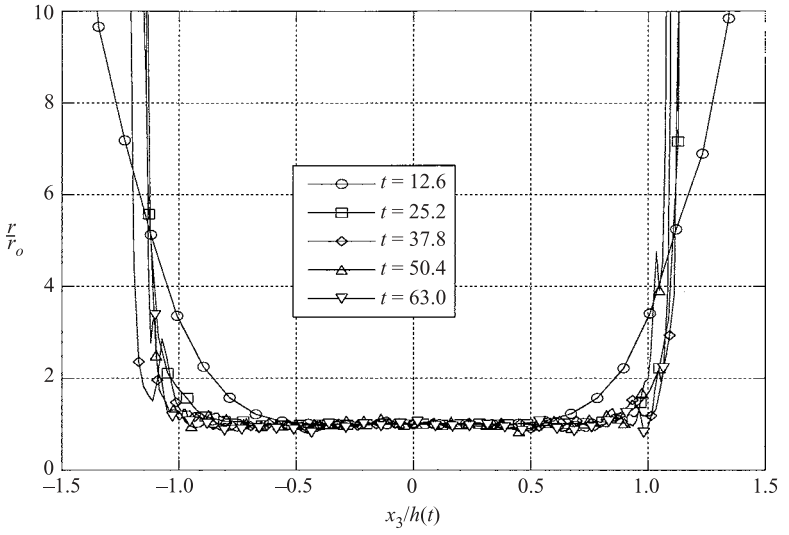

FIGURE 35. The time scale ratio profile.

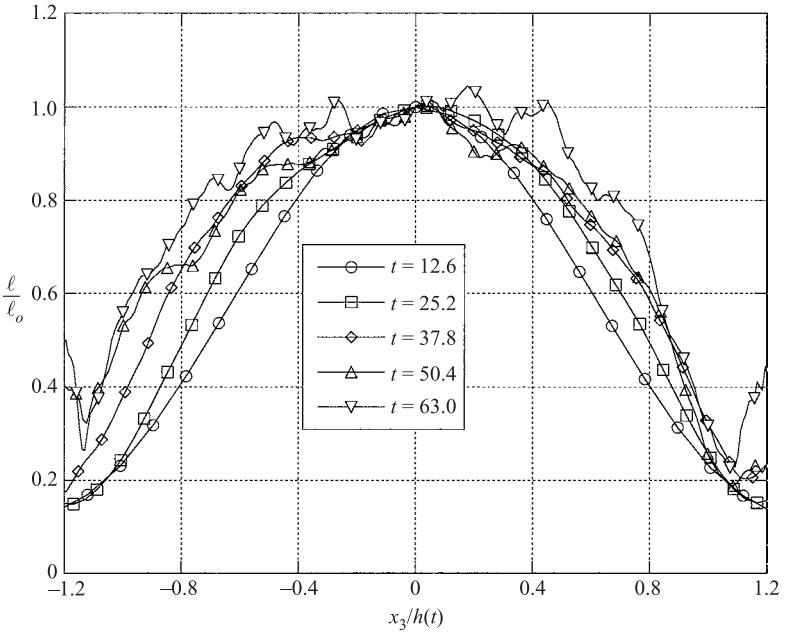

FIGURE 36. The energy-containing turbulence length scale, ℓ, profile.

6.4. *Spatial self-similarity of higher-order moments*

The velocity and concentration skewness, figures 39 and 40, are related to entrainment and their behaviour is expected to be important in inhomogeneous flows. The various kurtosis profiles are shown in figures 41 and 42. For self-similar flows the skewness and kurtosis are constants. This is clearly not the case for the edge regions. As higher-order moments are expected to reach a self-similar state at later time it may well be that the DNS has not continued long enough for these statistics. Close inspection of

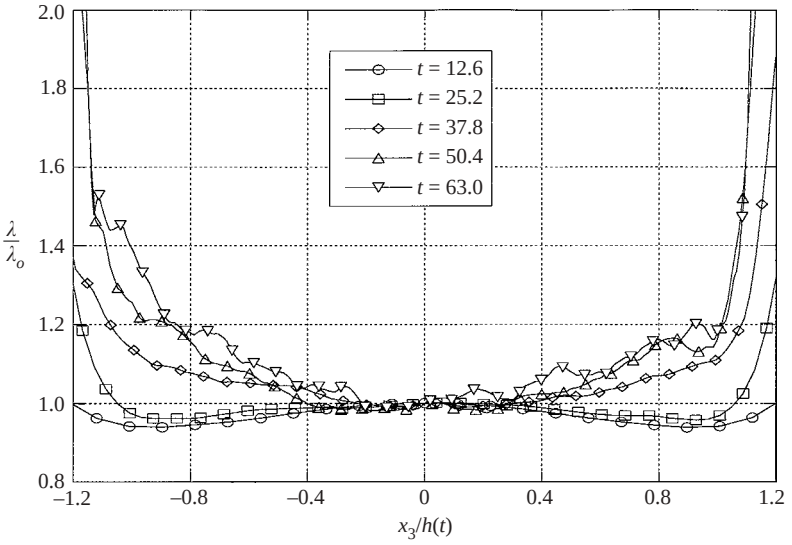

FIGURE 37. The velocity Taylor microscale, λ, profile.

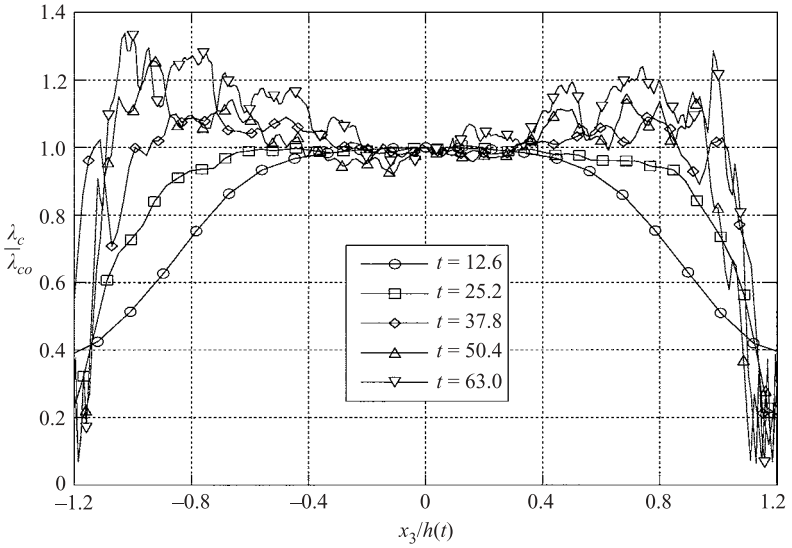

FIGURE 38. The scalar Taylor microscale, λ_c, profile.

the peaks of the skewness and kurtosis in the edge regions shows that the difference at successive times is less as the simulation proceeds.

6.5. *Summary of § 6 numerical results*

The moment profiles, when normalized by their current centreline values, collapse reasonably throughout the bulk of the layer. However, for the dissipations there are signficant departures from a spatial self-similarity, in the edge regions. This can be deduced from the production to dissipation ratios k/ε, r, λ and λ_c. Recall that the second-order moments in all these quantities have a self-similar collapse. The lack of self-similarity of quantities related to the dissipation appears consistent on two counts. A self-similar solution required the neglect of molecular transport effects in

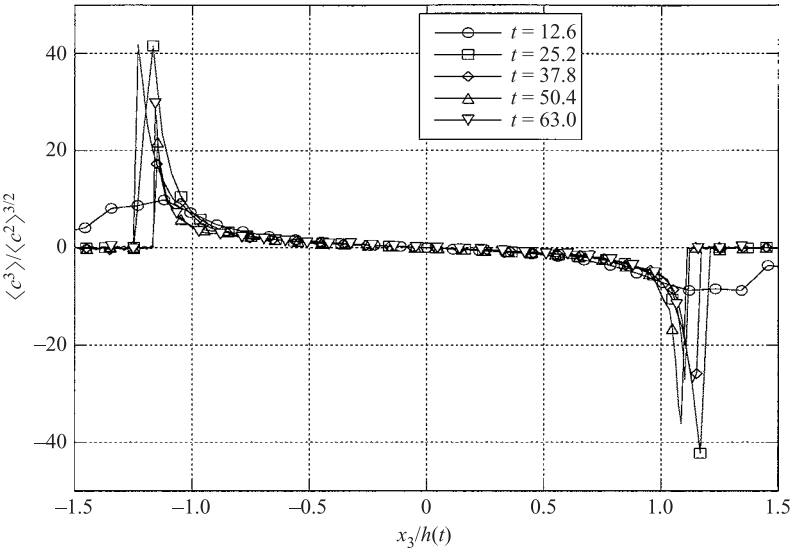

FIGURE 39. The scalar skewness profile.

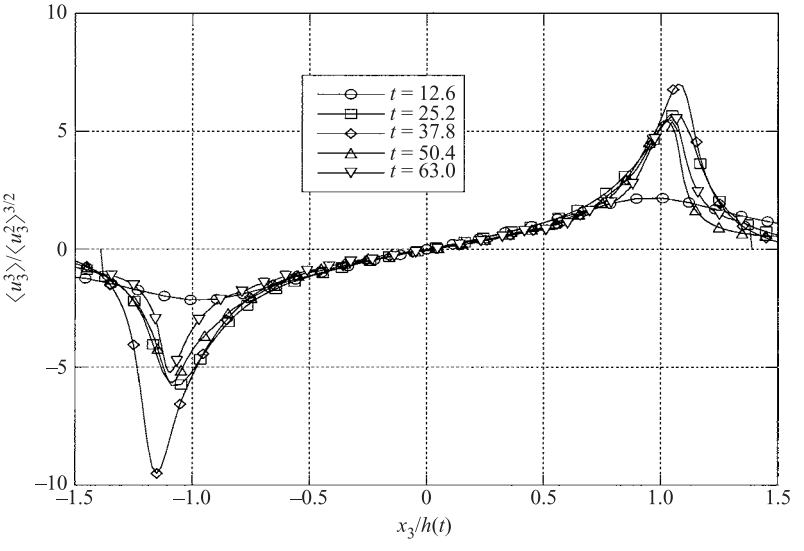

FIGURE 40. The vertical velocity skewness profile.

comparison to dissipation and this implies a high turbulence Reynolds number which is not true in the edge regions where the local turbulent Reynolds is very low and molecular transport may be important. As has been shown, a self-similar solution in the turbulence growth phase is only possible if molecular transport effects are ignored and this is unlikely to be physically realistic in the low-Reynolds-number edge regions. In addition the cascade ansatz for the dissipations is a high-Reynolds-number approximation. In addition there are highly significant departures, in the edge regions, from self-similarity for higher-order moments (kurtosis and skewness).

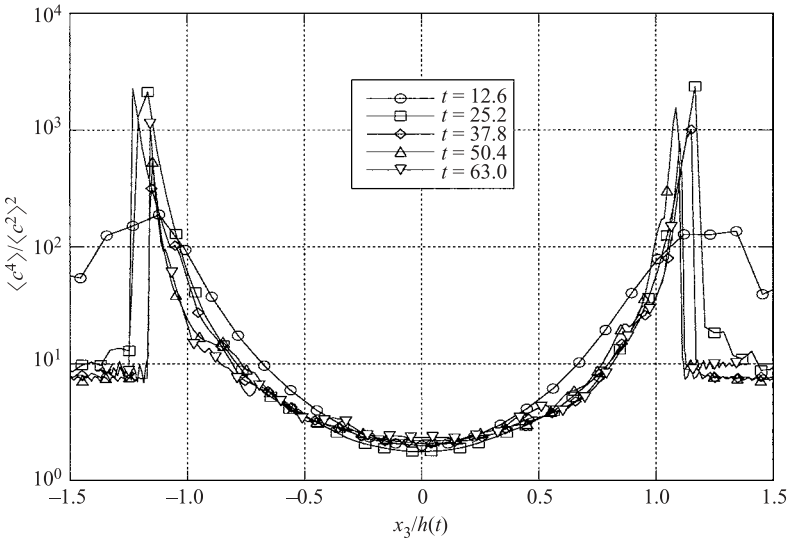

FIGURE 41. The scalar kurtosis profile.

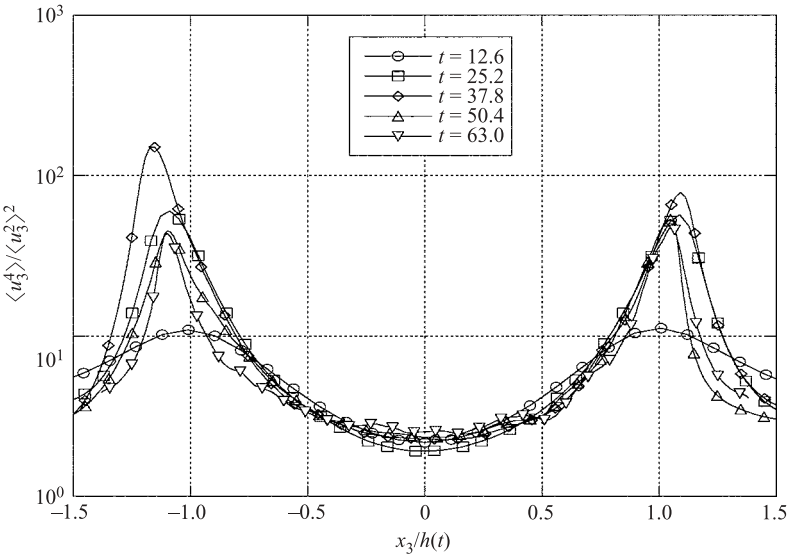

FIGURE 42. The vertical velocity kurtosis profile.

6.6. *Comparison with under-resolved simulations*

The possibility of using the DNS results, in which all scales of the motion are resolved, to verify coarse-grained numerical calculations of this flow is now discussed. The statistical properties of the flow that one might expect a course-grained numerical procedure to capture are those associated with the energy-containing ranges. The simplest are the second-order moments at the origin: $\langle cc\rangle_o$, $\langle u_3c\rangle_o$, $\langle u_3u_3\rangle_o$. The normalized moments at the origin, b_{33}, ρ_{3c}, Re_t, K_c, K_α, are expected to be accurately computable in a course-grained procedure.

Two basic turbulence parameters that measure the non-stationarity of the flow are the two production–dissipation ratios P/ε, P_c/ε_c. While one would not expect to capture the real dissipations, $\varepsilon, \varepsilon_c$, the production to the under-resolved dissipation provided by the LES model and the grid would have to match that shown in the figures above in order to capture accurately the non-equilibrium temporal behaviour of the energy-containing scales of the turbulence.

7. Summary

A self-similar analysis of the second-moment equations and a DNS of Rayleigh–Taylor turbulence has been conducted. Self-similarity is only possible with the neglect of molecular transport effects (which scale with Re^{-1}) while keeping the molecular dissipation effects. Such an assumption is only realistic for high Reynolds numbers and is therefore not applicable to the low-Reynolds-number edge regions where the most significant departures from self-similarity are seen in the DNS, § 6. The self-similar analysis describes the temporal evolution of the moments of the mixing layer appearing in the second-moment equations. In addition it produces an ordinary differential equation for the evolution of the planar-averaged mixing layer width whose solution is

$$\dot{h}^2 = Ag\, C_o h \qquad \Rightarrow \qquad h(t; C_o, h_0) = \tfrac{1}{4} Ag C_o t^2 + \sqrt{Ag C_o} h_0^{1/2} t + h_0$$

indicating that within the turbulence growth phase there is a short-time linear growth as well as a dependence on a virtual origin. The result is a rigorous consequence of the two ansatzen: self-similarity and Navier–Stokes equations (in the Boussinesq limit). The self-similar expression for $h(t; C_o, t_0)$ is well corroborated by the DNS. The analysis indicates that, even under the self-similar ansatz, the long-time asymptotic growth depends on C_o,

$$\alpha_{eff} = \frac{C_o}{4}\left(1 + \sqrt{\frac{4h_0}{Ag C_o t^2}}\right) \to \frac{C_o}{4},$$

a constant that is a function of the initial conditions. The above result is substantiated by the computations in which a decaying α is observed. It appears that the notion of a constant universal α is not supportable by either the self-similar analysis or the simulations for the low-Atwood-number Boussinesq flow. In practice C_o is a functional of the self-similar solution of the profiles in the unclosed set of second-moment equations which are independent of A.

While the focus of our study has not been the initial condition dependence of the flow (a subject of current research) a few observations appear pertinent. There is a statistically significant correlation between increasing n and decreasing α. A 20% difference in the mixing layer width and Reynolds numbers between the $n = 2$ and the $n = 6$ initial conditions is seen after seven eddy turnover times. The DNS indicate that the larger the amount of energy in the low wavenumbers of the initial spectra the higher the growth rate. This is consistent with the results of Cook & Dimotakis (2001) as can be inferred from their figures 2, 6, and 8. It is not possible conclude whether the low-wavenumber exponent or the relative spectral peak effect, as proposed by Cook & Dimotakis (2001), is more important. Given the observations of Linden *et al.* (1994) and Dalziel *et al.* (1999) one expects that the presence of a deterministic large-scale structure in the initial conditions would have a sizeable effect on, at least, the mixing layer growth rate.

Four turbulence length scales have three different temporal scalings. The largest turbulence length scale grows as t^2 while the smallest length scale shrinks as $t^{-1/4}$. An intermediate scale characteristic of mixing structures grows as $t^{1/2}$. In the self-similar regime the four turbulence lengths scale with different powers of the mixing layer width according to

$$\ell_o \sim h(t; C_o, h_0), \quad \lambda_o \sim h^{1/4}(t; C_o, h_0), \quad \lambda_{co} \sim h^{1/4}(t; C_o, h_0), \quad \eta_o \sim h^{-1/8}(t; C_o, h_0).$$

The self-similar expressions for the scalings of the turbulence lengths are corroborated by the DNS within three initial eddy turnover times of the inception of the turbulence growth phase. At this time $Re \approx 700$–1000 and $Re_{to} \approx 100$–150. Consistent with these results is the noteworthy fact that the Kolmogorov scalings $\eta_o/\ell_o \sim Re_t^{-3/4}(t)$ and $\lambda_o/\ell_o \sim Re_t^{-1/2}(t)$ (Tennekes & Lumley 1972), thought to be a consequence of the stationarity of the spectral flux through the inertial range are valid for non-stationary turbulence. The turbulence bandwidth at the centreline, $\approx \ell_o/\eta_o$, expands as

$$\frac{\ell_o}{\eta_o} \sim \left(\frac{(AgC_o)^6}{2\nu^3}\right)^{1/4} (t_0(\tau+1))^{9/4} \sim Re_t^{3/4}(t; C_o, t_0) \sim h^{9/8}(t; C_o, t_0).$$

From a computational point of view this is bad news: the smaller scales are getting smaller all the time. In a doubling of the flow time there is a fivefold increase in spectral bandwidth. This is due to the ever increasing Reynolds number from the buoyancy forcing and the non-stationarity of the cascade. All the aforementioned self-similar scaling features of the turbulence length scales are corroborated by DNS.

There is consistency between the DNS and the self-similar results for the scalar and velocity variances, particularly after about five initial eddy turnovers and $Re > 1500$ and $Re_{to} > 250$. The same cannot be said for any arbitrary moment appearing in the second-order moment equations. For example the scalar flux or the three dissipations can only be said to be approaching the self-similar prediction at late time. This may well be due to low Reynolds number in as much as the cascade scaling assumed for the dissipations requires a high Reynolds number. The scalar kurtosis, at the origin, does not become stationary and is expected, from what is known of isotropic homogeneous turbulence, to continue to increase due to intermittency. In as much as the flow has evolved for several eddy turnover times and the cubic nonlinearities in the second-moment equations are fully developed it does not appear possible to conclude that a comprehensive moment self-similarity can be assumed for the Rayleigh–Taylor mixing layer. This is especially true in the edge regions for the dissipation statistics where the low Reynolds number suggests that the cascade scaling for the dissipations is unlikely and molecular transport not negligible and thus the self-similar turbulence ansatz invalid.

It does appear possible to conclude that: (i) Any quantitative description of the mixing layer width growth in the turbulence growth phase includes a linear regime and a virtual origin. (ii) α is not a universal constant and is a functional of the spatial solution of the unclosed second-moment equations. (iii) The turbulence length scales evolve as some power of $h(t; C_o, h_0)$ and are in accord with Kolmogorov scalings. (iv) There is a statistically significant correlation between between decreasing α and decreasing low-wavenumber loading of the initial spectrum. (v) The whole mixing layer cannot be self-similar due to the importance of molecular effects in the low-Reynolds-number edge region. (vi) At no time and in no location is the layer fully molecularly mixed.

C. W. Cranfill is thanked for pointing out some key issues regarding self-similar analyses which have contributed significantly to the self-similar results. This work was performed under the auspices of the US Department of Energy by the Los Alamos National Laboratory under contract number W-7405-ENG-36.

Appendix. Method of numerical simulation and initial conditions

The numerical solution procedure is now described. Details regarding the finite Fourier transform method in the homogeneous directions are given. The method of numerical solution is presented and the initial conditions discussed. The Boussinesq equations have been described in an earlier section. In dimensional form the simulation procedure uses the following form of the momentum equation:

$$\frac{\partial u_i^*}{\partial t} + \epsilon_{ijk}\omega_j^* u_k^* = Ag_i c^* - p^*{}_{,i} + \nu u_i^*{}_{,jj} \tag{A 1}$$

where $p^* = p + u_n^* u_n^*/2$. Consider the case where the acceleration acts only in the x_3-direction. The u_3 equation is

$$\frac{\partial u_3^*}{\partial t} + \epsilon_{3jk}\omega_j^* u_k^* = -Ag_3 c^* - p^*{}_{,i} + \nu u_i^*{}_{,jj}. \tag{A 2}$$

Averaging the above equation over x_2 and x_1, where $\langle u_3^* \rangle = U_3$, yields

$$\frac{\partial U_3}{\partial t} + \epsilon_{3jk}\langle \omega_j^* u_k^* \rangle = -Ag_3 C - P_{,3} + \nu U_{3,jj}. \tag{A 3}$$

As the fluid is incompressible the volumetric flux in the x_3-direction is zero so $U_3 = 0$, and the mean pressure gradient is given by

$$-P_{,3} = +Ag_3 C + \epsilon_{3jk}\langle \omega_j^* u_k^* \rangle \tag{A 4}$$

where $p^* = P + p$ and $c^* = C + c$. Thus

$$P(x_3) = -\int_{x_3} \{Ag_3 C + \epsilon_{3jk}\langle \omega_j^* u_k^* \rangle\}\, \mathrm{d}x_3. \tag{A 5}$$

Noting that $u_3^* = u_3$, the u_3 equation can be written

$$\frac{\partial u_3}{\partial t} + \epsilon_{3jk}(\omega_j u_k - \langle \omega_j u_k \rangle) = Ag_3 c - p_{,3} + \nu u_{3,jj}. \tag{A 6}$$

The u_2 and u_3 (generically u_α) equations are

$$\frac{\partial u_\alpha}{\partial t} + \epsilon_{\alpha jk}(\omega_j u_k - \langle \omega_j u_k \rangle) = -p_{,\alpha} + \nu u_{\alpha,jj}. \tag{A 7}$$

The boundary conditions for the present simulations are stress-free boundaries at the top ($x_3 = 0$) and bottom ($x_3 = \pi$) of the domain and periodic in x_1 and x_2. The fluctuating pressure boundary condition devolves to

$$\frac{\partial p}{\partial x_3}_{x_3 = 0,\pi} = Ag_3 c. \tag{A 8}$$

The divergence of the momentum equation gives the fluctuating pressure–Poisson equation,

$$-\frac{\partial^2 p}{\partial x_i \partial x_i} = \epsilon_{ijk}(\omega_j u_k - \delta_{i3}\langle \omega_j u_k \rangle)_{,i} - Ag_3 c_{,3}. \tag{A 9}$$

These equations are solved using a spectral method with the following representations:

$$u_3(\boldsymbol{x},t)=\sum_{\boldsymbol{k}}^{N}\hat{u}_3(\boldsymbol{k},t)F_s(\boldsymbol{k},\boldsymbol{x}),\qquad c^*(\boldsymbol{x},t)=\sum_{\boldsymbol{k}}^{N}\hat{c}^*(\boldsymbol{k},t)F_c(\boldsymbol{k},\boldsymbol{x}),\tag{A 10}$$

$$u_1(\boldsymbol{x},t)=\sum_{\boldsymbol{k}}^{N}\hat{u}_1(\boldsymbol{k},t)F_c(\boldsymbol{k},\boldsymbol{x}),\qquad u_2(\boldsymbol{x},t)=\sum_{\boldsymbol{k}}^{N}\hat{u}_2(\boldsymbol{k},t)F_c(\boldsymbol{k},\boldsymbol{x}),\tag{A 11}$$

where

$$F_s(\boldsymbol{k},\boldsymbol{x})=\sin(k_3x_3)\mathrm{e}^{\mathrm{i}k_1x_1}\mathrm{e}^{\mathrm{i}k_2x_2},\qquad F_c(\boldsymbol{k},\boldsymbol{x})=\cos(k_3x_3)\mathrm{e}^{\mathrm{i}k_1x_1}\mathrm{e}^{\mathrm{i}k_2x_2}.\tag{A 12}$$

The total concentration will be decomposed into mean and fluctuating spectral parts in § A.1. Unfortunately, the pressure requires a mixed sine–cosine representation. The pressure is treated as two separate entities, $p=p_c+p_s$; one part expressible in terms of $F_c(\boldsymbol{k},\mathbf{x})$ and the other in terms of $F_s(\boldsymbol{k},\boldsymbol{x})$. These must satisfy their corresponding Poisson equations:

$$-\frac{\partial^2 p_s}{\partial x_i\partial x_i}=-Ag_3\frac{\partial c}{\partial x_3},\tag{A 13}$$

$$-\frac{\partial^2 p_c}{\partial x_i\partial x_i}=\epsilon_{3jk}\frac{\partial(\omega_j u_k-\langle\omega_j u_k\rangle)}{\partial x_3}+\epsilon_{1jk}\frac{\partial\omega_j u_k}{\partial x_1}+\epsilon_{2jk}\frac{\partial\omega_j u_k}{\partial x_2}.\tag{A 14}$$

The nonlinear advection terms are computed using pseudo-spectral techniques. Their transforms are denoted by

$$\hat{f}_3(\boldsymbol{k})=\epsilon_{3jk}\sum_{\boldsymbol{x}}^{N}[\omega_j u_k-\langle\omega_j u_k\rangle]F_s(\boldsymbol{x},\boldsymbol{k}),\tag{A 15}$$

$$\hat{f}_2(\boldsymbol{k})=\epsilon_{2jk}\sum_{\boldsymbol{x}}^{N}[\omega_j u_k]F_c(\boldsymbol{x},\boldsymbol{k}),\tag{A 16}$$

$$\hat{f}_1(\boldsymbol{k})=\epsilon_{1jk}\sum_{\boldsymbol{x}}^{N}[\omega_j u_k]F_c(\boldsymbol{x},\boldsymbol{k}).\tag{A 17}$$

The pressure equations for the cosine part and for the sine parts are

$$\hat{p}_c(\boldsymbol{k})=\frac{1}{k^2}\{k_3\hat{f}_3(\boldsymbol{k})+ik_2\hat{f}_2(\boldsymbol{k})+ik_1\hat{f}_1(\boldsymbol{k})\},\qquad \hat{p}_s(\boldsymbol{k})=\frac{k_3}{k^2}Ag_3\hat{c}(\boldsymbol{k}).\tag{A 18}$$

Note that the x_3-gradient of p_s and the accelerative terms Ag_3c must be expressed as cosine functions. These two terms are combined in the u_3-equation and the result projected onto a sine representation. Letting

$$\left.\begin{aligned}\pi_c(\boldsymbol{k})&=-(k_3\hat{p}_s(\boldsymbol{k}))+Ag_3\hat{c}(\boldsymbol{k})=-\frac{k_3^2}{k^2}Ag_3\hat{c}(\boldsymbol{k})+Ag_3\hat{c}(\boldsymbol{k})=\left\{1-\frac{k_1^2}{k^2}\right\}A_tg_3\hat{c}(\boldsymbol{k})\\ \pi_s(\boldsymbol{k})&=-(-k_3\hat{p}_c(\boldsymbol{k}))=k_3\hat{p}_c(\boldsymbol{k}),\end{aligned}\right\}\tag{A 19}$$

the x_3 velocity equation becomes

$$\frac{\partial}{\partial t}\sum_{\boldsymbol{q}}^{N}\hat{u}_3(\boldsymbol{q})F_s(\boldsymbol{x},\boldsymbol{q})+\nu q^2\sum_{\boldsymbol{q}}^{N}\hat{u}_3(\boldsymbol{q})F_s(\boldsymbol{x},\boldsymbol{q})=-\sum_{\boldsymbol{q}}^{N}\hat{f}_3(\boldsymbol{q})F_s(\boldsymbol{x},\boldsymbol{q})+\sum_{\boldsymbol{q}}^{N}\pi_s(\boldsymbol{q})F_s(\boldsymbol{x},\boldsymbol{q})+\sum_{\boldsymbol{q}}^{N}\pi_c(\boldsymbol{q})F_c(\boldsymbol{x},\boldsymbol{q}).\tag{A 20}$$

Multiplying through by $F_s^{-1}(\boldsymbol{x}, \boldsymbol{k})$ and summing over all $\boldsymbol{x}$ gives

$$\frac{\partial}{\partial t}\hat{u}_3(\boldsymbol{k}) + \nu k^2 \hat{u}_3(\boldsymbol{k}) = -\hat{f}_3(\boldsymbol{k}) + \pi_s(\boldsymbol{k}) + \sum_{\boldsymbol{x}}^{N}\sum_{\boldsymbol{q}}^{N} \pi_c(\boldsymbol{q}) F_c(\boldsymbol{x}, \boldsymbol{q}) F_s(\boldsymbol{x}, \boldsymbol{k}). \quad \text{(A 21)}$$

The double sum in this equation is evaluated by transforming to configuration space using an inverse cosine transform and transforming back using a forward sine tranform. The last term will be written $\pi_{s\to c}(\boldsymbol{k})$. The u_1 and u_2 equations are arrived at using similar reasoning:

$$\frac{\partial \hat{u}_1(\boldsymbol{k})}{\partial t} + \nu k^2 \hat{u}_1(\boldsymbol{k}) = -\hat{f}_1(\boldsymbol{k}) - \mathrm{i}k_1 \hat{p}_c(\boldsymbol{k}) - \mathrm{i}k_1 \hat{p}_{s\to c}(\boldsymbol{k}), \quad \text{(A 22)}$$

$$\frac{\partial \hat{u}_2(\boldsymbol{k})}{\partial t} + \nu k^2 \hat{u}_2(\boldsymbol{k}) = -\hat{f}_2(\boldsymbol{k}) - \mathrm{i}k_2 \hat{p}_c(\boldsymbol{k}) - \mathrm{i}k_2 \hat{p}_{s\to c}(\boldsymbol{k}). \quad \text{(A 23)}$$

Taking the divergence of the three velocity equations yields

$$\begin{aligned} \Delta = -k_1 \hat{f}_1(\boldsymbol{k}) + k_1^2 \hat{p}_c(\boldsymbol{k}) + k_1 \pi_{c\to s}(\boldsymbol{k}) - \mathrm{i}k_2 \hat{f}_2(\boldsymbol{k}) + k_2^2[\hat{p}_c(\boldsymbol{k}) + \hat{p}_{s\to c}(\boldsymbol{k})] \\ - \mathrm{i}k_3 \hat{f}_3(\boldsymbol{k}) + k_3^2[\hat{p}_c(\boldsymbol{k}) + \hat{p}_{s\to c}(\boldsymbol{k})] \quad \text{(A 24)} \end{aligned}$$

or, rearranging,

$$\Delta + k_1 \hat{f}_1(\boldsymbol{k}) + \mathrm{i}k_3 \hat{f}_3(\boldsymbol{k}) + \mathrm{i}k_2 \hat{f}_2(\boldsymbol{k}) = k^2 \hat{p}_c(\boldsymbol{k}) + k_1 \pi_{c\to s}(\boldsymbol{k}) + k_2^2 \hat{p}_{s\to c}(\boldsymbol{k}) + k_3^2 \hat{p}_{s\to c}(\boldsymbol{k}),$$

or finally, from our definition of $\hat{p}_c$, we conclude that

$$\Delta = k_1 \pi_{c\to s}(\boldsymbol{k}) + \left(k_2^2 + k_3^2\right) \hat{p}_{s\to c}(\boldsymbol{k}) \quad \text{(A 25)}$$

which is a relation between $\pi_{c\to s}(\boldsymbol{k})$ and $\hat{p}_{s\to c}(\boldsymbol{k})$ since the divergence is zero.

A.1. *The concentration equation*

The concentration equation

$$\frac{\partial}{\partial t} c^* + u_j^* c^*{}_{,j} = \mathscr{D}\, c^*{}_{,jj} \quad \text{(A 26)}$$

can be written in terms of two equations following the usual Reynolds decomposition, $c^* = C + c$,

$$\frac{\partial C}{\partial t} + \frac{\partial \langle u_3 c \rangle}{\partial x_3} = \mathscr{D} \frac{\partial^2 C}{\partial x_3 \partial x_3}. \quad \text{(A 27)}$$

$$\frac{\partial c}{\partial t} + \frac{\partial u_n c}{\partial x_n} + u_3 \frac{\partial C}{\partial x_3} - \frac{\partial \langle u_3 c \rangle}{\partial x_3} = \mathscr{D} \frac{\partial^2 c}{\partial x_n \partial x_n}. \quad \text{(A 28)}$$

The spectral equation for the mean concentration (A 27) becomes

$$\frac{\partial \hat{C}(k_3)}{\partial t} + \mathscr{D} k_3^2 \hat{C}(k_3) = -k_3 \hat{M}_1(k_3) \quad \text{(A 29)}$$

where

$$\langle u_3 c \rangle = \sum_{k_3} \hat{M}_1(k_3, t) \sin(k_3 x_3) \quad \text{(A 30)}$$

is a sine expansion since u_1 and c are odd (sine) and even (cosine) functions; the product is expressible in terms of 'odd' (sine) functions.

Next is a difficult issue regarding the treatment of the flux and production terms when the spectral representation of (A 28) is undertaken. Let

$$u_3(\boldsymbol{x}, t)c(\boldsymbol{x}, t) = \sum_{\boldsymbol{k}} \hat{m}_3(\boldsymbol{k}, t)F_s(\boldsymbol{k}, \boldsymbol{x}), \tag{A 31}$$

$$u_2(\boldsymbol{x}, t)c(\boldsymbol{x}, t) = \sum_{\boldsymbol{k}} \hat{m}_2(\boldsymbol{k}, t)F_c(\boldsymbol{k}, \boldsymbol{x}), \tag{A 32}$$

$$u_1(\boldsymbol{x}, t)c(\boldsymbol{x}, t) = \sum_{\boldsymbol{k}} \hat{m}_1(\boldsymbol{k}, t)F_c(\boldsymbol{k}, \boldsymbol{x}), \tag{A 33}$$

and

$$u_3(\boldsymbol{x}, t)C(x_3, t) = \sum_{\boldsymbol{k}} \hat{n}_3(\boldsymbol{k}, t)F_s(\boldsymbol{k}, \boldsymbol{x}), \tag{A 34}$$

$$u_2(\boldsymbol{x}, t)C(x_3, t) = \sum_{\boldsymbol{k}} \hat{n}_2(\boldsymbol{k}, t)F_c(\boldsymbol{k}, \boldsymbol{x}), \tag{A 35}$$

$$u_1(\boldsymbol{x}, t)C(x_3, t) = \sum_{\boldsymbol{k}} \hat{n}_1(\boldsymbol{k}, t)F_c(\boldsymbol{k}, \boldsymbol{x}). \tag{A 36}$$

The spectral equation for the fluctuating concentration (A 28) becomes

$$\begin{aligned}\frac{\partial}{\partial t}\sum_{\boldsymbol{k}}^{N} \hat{c}(\boldsymbol{k}, \boldsymbol{t})F_c(\boldsymbol{x}, \boldsymbol{k}) + \mathscr{D}k^2 \sum_{\boldsymbol{q}}^{N} \hat{c}(\boldsymbol{k}, \boldsymbol{t})F_c(\boldsymbol{x}, \boldsymbol{k}) &= k_3 \sum_{\boldsymbol{k}}^{N} \hat{n}_3(\boldsymbol{q})F_c(\boldsymbol{x}, \boldsymbol{k}) \\ &+ k_3 \sum_{k_3} \hat{M}_1(k_3, t)\cos(k_3 x_3) - k_3 \sum_{\boldsymbol{k}}^{N} \hat{m}_3(\boldsymbol{k})F_c(\boldsymbol{x}, \boldsymbol{k}) \\ &- \mathrm{i}k_1 \sum_{\boldsymbol{k}}^{N} \hat{m}_1(\boldsymbol{k})F_c(\boldsymbol{x}, \boldsymbol{k}) - \mathrm{i}k_2 \sum_{\boldsymbol{k}}^{N} \hat{m}_2(\boldsymbol{k})F_c(\boldsymbol{x}, \boldsymbol{k}),\end{aligned} \tag{A 37}$$

the right-hand side being, respectively, the production term, and the divergence of the planar-average concentration flux minus the divergence of the instantaneous flux of (A 28). The basis functions are all cosines and summing over x as done above produces the final equation solved.

A.2. *Numerical procedure*

The time advancement of the system of spectral equations is accomplished with a fourth-order Runge–Kutta scheme, see Burden, Faires & Reynolds (1981). The viscous and diffusive terms are treated using 'exact integration' as discussed by Canuto *et al.* (1987). The calculations are fully dealiased by using a set of four phase-shifts ('original' phase plus three additional shifts, see for example Canuto *et al.* (1987)) in the periodic directions and a one-third truncation in the aperiodic direction. Full dealiasing was applied at every stage of the Runge–Kutta time advancement. The Runge–Kutta algorithm permits variable time-step sizes. The time-steps are set to the smallest of a Courant–Fredrich–Levy (CFL) criterion of one-quarter or a value of $\Delta_t = 10^{-3}$.

A.3. *The initial conditions*

As the physical problem typically has stochastic initial conditions a stochastic initial condition is chosen. The discontinuity of the initial concentration field, for the physical problem, prohibits its use as an initial condition for this class of numerical simulation. As consequence the following reasonable and realizable stochastic function is chosen

as the initial condition:

$$c^*(x, y, z, 0) = \tanh\left(\frac{z}{\delta} + \xi(x, y)\right). \tag{A 38}$$

The stochastic process ξ is given by

$$\xi = \Sigma A_n(\kappa) e^{\mathrm{i}(\kappa_j x_j + \theta)} \tag{A 39}$$

where $j = 1, 2$ and where θ is the uniformly distributed over $[0, 2\pi]$. The spectrum of the initial concentration fluctuations is given by

$$E_n(\kappa) = \langle \xi\xi \rangle_o \frac{\left(\dfrac{\kappa}{\kappa_c}\right)^n \exp\left(-\dfrac{1}{2}a\left(\dfrac{\kappa}{\kappa_c}\right)^2\right)}{\displaystyle\int_0^\infty \left(\frac{\kappa}{\kappa_c}\right)^n \exp\left(-\frac{1}{2}a\left(\frac{\kappa}{\kappa_c}\right)^2\right) \mathrm{d}\kappa}. \tag{A 40}$$

There are eleven simulations. All the simulations have $a = n$ and therefore the peak of the initial spectrum at always at the same location. All the simulations have the same initial interfacial variance coresponding $\langle \xi\xi \rangle_o = 0.25$ of the grid spacing. There are 300 grid points in the inhomogeneous direction and 150 in each of the homogeneous directions. The Atwood and Schmidt numbers are $A = 0.01$, $Sc = 1$, in all simulations.

There is one simulation, with $n = 6$, that is much longer than the others; in this simulation the acceleration is four times larger. It has been run to verify that different behaviour does not set in at later time. At late time the lack of monotonicity in the bulk Reynolds number (and other statistics below) is due to two effects: (i) the approach of the mixing layer edge to the end of the computational domain and (ii) the ever decreasing sample size at the edge of the layer where the data are increasing intermittent. The simulations are stopped once end effects become apparent.

REFERENCES

de Bruyn Kops, S. M. & Riley, J. J. 2000 Re-examining the thermal mixing layer with numerical simulations. *Phys. Fluids* A **12**, 185–192.

Burden, R. L., Faires, J. D. & Reynolds, A. C. 1981 *Numerical Analysis*, Second Edn, pp. 205–206. Prindle, Weber and Schmidt, Boston.

Canuto, C., Hussaini, M. Y., Quarteroni, A. & Zang, T. A. 1987 *Spectral Methods in Fluid Dynamics*, pp. 112–113 Springer.

Clark, T. T. & Zhou, Y. 2001 Growth rate exponents of Richtmyer-Meshkov mixing layers. *Los Alamos National Laboratory Unclassified Rep.* LA-UR-01-5392

Clark, T. T. & Zhou, Y. 2003 Self-similarity of two flows induced by instabilities. *Phys. Rev.* E **66**, 66305-1-16.

Cook, A. W. & Dimotakis, P. E. 2001 Transition stages of Rayleigh-Taylor instability between miscible fluids. *J. Fluid Mech.* **443**, 69–99.

Chandrasekhar, S. 1961 *Hydrodynamic and Hydromagnetic Stability*. University Press, London.

Daziel, S. B., Linden, P. F. & Youngs, D. L. 1999 Self-similarity and internal structure of turbulence induced by Rayleigh-Taylor instability. *J. Fluid Mech.* **399**, 1–48.

Dimonte, G. & Schneider, M. 2000 Density ratio dependence of Rayleigh-Taylor mixing for sustained and impulsive acceleration histories. *Phys Fluids* **12**, 304–312.

Fermi, E. 1951 Taylor instability at the boundary of two incompressible fluids. *The Collected Papers of Enrico Fermi*, vol 2 (ed. E. Segre).

Gauthier, S. & Bonnet, M. 1990 A $k-\epsilon$ model for turbulent mixing in shock-tube flows induced by Rayleigh-Taylor instability. *Phys Fluids* A **2**, 1685–1694.

Linden, P. F. & Redondo, J. M. 1991 Molecular mixing in Rayleigh-Taylor instability. Part I: global mixing. *Phys. Fluids* A **3**, 1269–1277.

Linden, P. F., Redondo, J. M. & Youngs, D. L. 1994 Molecular mixing in Rayleigh-Taylor instability. *J. Fluid Mech.* **265**, 97–124.

Lumley, J. L. 1978 Computational modeling of turbulent flows. *Adv. Appl. Mech.* **18**, 123.

Lumley, J. L. 1986 Evolution of the non-self-preserving thermal mixing layer. *Phys. Fluids* A **29**, 3976–3982.

Ma, B.-K. & Warhaft, Z. 1986 Some aspects of the thermal mixing layer in grid turbulence. *Phys. Fluids* A **29**, 3114–3124.

Mohamed, M. S. & LaRue, J. C. 1990 The decay power law in grid generated turbulence. *J. Fluid Mech.* **219**, 195–214.

Pope, S. B. 2000 *Turbulent Flows*. Cambridge University Press.

Sharp, D. H. 1984 An overview of the Rayleigh-Taylor instability. *Physica* D **12**, 3–18.

Snider, D. M. & Andrews, M. J. 1994 Rayleigh-Taylor and shear driven mixing with unstable thermal stratification. *Phys. Fluids* A **6**, 3324–3334.

Tennekes, H. & Lumley, J. L. 1972 *A First Course in Turbulence*. MIT Press.

Town, R. J. P. & Bell, A. R. 1991 Three dimensional simulations of the implosion of inertial confinement targets. *Phys. Rev. Lett.* **67**, 1863–1866.

Wilson, P. N. & Andrews, M. J. 2002 Spectral measurements of Rayleigh–Taylor mixing at small Atwood number. *Phys. Fluids* **14**, 938–945.

Youngs, D. L. 1984 Numerical simulation of turbulent mixing by Rayleigh-Taylor instability. *Physica* D **12**, 32–44.

Youngs, D. L. 1989 Modelling turbulent mixing by Rayleigh-Taylor instability. *Physica* D **37**, 270–287.

Youngs, D. L. 1994 Numerical simulation of mixing in Rayleigh-Taylor and Richtmeyer-Meshkov instabilities. *Laser and Particle Beams* **12**, 725–750.

Youngs, D. L. 1991 Three dimensional numerical simulation of turbulent mixing by Rayleigh-Taylor instabilities. *Phys Fluids* A **3**, 1312–1320.

Young, Y.-N., Tufo, H., Dubey, A. & Rosner, R. 2001 On the miscible Rayleigh-Taylor instability: two and three dimensions. *J. Fluid Mech.* **447**, 377–408.